PPPL-2197 (2)

UC20-G

PPPL-2197

THEORY AND SIMULATIONS OF CURRENT DRIVE VIA INJECTION OF AN ELECTRON BEAM IN THE ACT-1 DEVICE

By

H. Okuda, R. Horton, M. Ono, and K.L. Wong

FEBRUARY 1985

PLASMA PHYSICS LABORATORY

PRINCETON UNIVERSITY

PRINCETON, NEW JERSEY

PREPARED FOR THE U.S. DEPARTMENT OF ENERGY,
UNDER CONTRACT DE-AC02-76-CHO-3073.

THEORY AND SIMULATIONS OF CURRENT DRIVE VIA INJECTION OF AN ELECTRON BEAM IN THE ACT-1 DEVICE

PPPL--2197

DE85 008717

H. Okuda, R. Horton, M. Ono, and K.L. Wong

Plasma Physics Laboratory, Princeton University

Princeton, NJ 08544

ABSTRACT

One- and two-dimensional particle simulations of beam-plasma interaction have been carried out in order to understand current drive experiments that use an electron beam injected into the ACT-1 device. Typically, the beam velocity along the magnetic field is $V = 10^9$ cm/sec while the thermal velocity of the background electrons is $v_t = 10^8$/cm. The ratio of the beam density to the background density is about 10% so that a strong beam-plasma instability develops causing rapid diffusion of beam particles. For both one- and two-dimensional simulations, it is found that a significant amount of beam and background electrons is accelerated considerably beyond the initial beam velocity when the beam density is more than a few percent of the background plasma density. In addition, electron distribution along the magnetic field has a smooth negative slope, $f'(v_\parallel) < 0$, for $v_\parallel > 0$ extending $v_\parallel = 1.5\ V \sim 2\ V$, which is in sharp contrast to the predictions from quasilinear theory. An estimate of the mean-free path for beam electrons due to Coulomb collisions reveals that the beam electrons can propagate a much longer distance than is predicted from a quasilinear theory, due to the presence of a high energy tail. These simulation results agree well with the experimental observations from the ACT-1 device.

I. INTRODUCTION

Current drive in a toroidal device is important in relation to steady-state operation of a tokamak device. Various schemes including relativistic electron beam injection,[1] use of electromagnetic waves,[2,3] and synchrotron radiation spontaneously generated in a plasma[4] have been proposed.

For the case of the electron beam injection experiment, such as done in the ACT-1 device,[5] it is important to consider the effects of beam-plasma interactions in determining the beam distribution and the resultant current drive. This is because the beam density is relatively high compared with the background plasma density so that strong electrostatic instabilities associated with beam-plasma interaction develop, thereby modifying both the beam and the background electron distributions. An application of a quasilinear theory[6,7] and the Coulomb collision theory to determine the current generation indicates that the current generated by the electron beam is too small to explain the observations in the ACT-1 device.[5] This discrepancy may be traced to the fact that the velocity distribution with a plateau predicted from a quasilinear theory[6] does not agree with experimental observations where a high energy tail whose velocity significantly exceeds the initial beam velocity has been observed.[5]

There have been a number of nonlinear theories for the beam-plasma instability. Nonlinear saturation of the instability is calculated within the framework of quasilinear theory,[6,7] which is valid in the presence of many unstable modes so that the coherent trapping of particles is not important. When only a single mode is unstable, a nonlinear theory is developed when the beam density is much smaller than the background density.[8]

When the beam density is high, for example, more than a few percent of the background plasma, several modes become highly nonlinear so that particle

trapping becomes very important. Under such conditions no appropriate nonlinear theory has been developed.

There are several computer simulation studies on the beam-plasma instabilities[9-11] using a one-dimensional model. In these calculations, development of large amplitude waves and the associated particle distributions are studied. In these works, it is found that the trapping of particles plays an important role in the nonlinear development of the beam-plasma instability.

In the present work, we shall study the beam-plasma instabilities first using a one-dimensional electrostatic model in a uniform external magnetic field B_o which corresponds to an electron beam of infinite transverse extent. Both parallel ($k \times B_o = 0$) and oblique ($k \times B_o \neq 0$) propagations are studied. Simulations are extended to two dimensions where effects of the finite radius of the electron beam can be incorporated. Using the beam velocity distribution obtained in the simulation, an estimate of the mean-free path due to Coulomb collisions is obtained to compare with the experimental observation in the ACT-1 device.

In Sec. II, we shall briefly review the theory of beam-plasma instabilities in the electrostatic limit. In Sec. III, simulation results from one-dimensional models are given for different beam density and velocity for parallel ($k \times B_o = 0$) and oblique ($k \times B_o \neq 0$) propagations. Two-dimensional simulations are given in Sec. IV and are compared with one-dimensional results. Conclusions are given in Sec. V along with suggestions for future research.

II. LINEAR THEORY

Consider a beam-plasma system in which an electron beam is drifting along a uniform magnetic field in a uniform background plasma. When the drift speed of the beam is large in comparison with the thermal speeds of both the beam and background electrons, one may use a cold plasma dispersion relation to describe small amplitude waves. In the limit of electrostatic approximation, relevant to the ACT-1 device one finds for $\underset{\sim}{k} = (0, k_y, k_z)$,

$$1 = (1-\varepsilon)\left(\frac{k_y^2}{k^2}\frac{\omega_{pe}^2}{\omega^2-\Omega_e^2} + \frac{k_z^2}{k^2}\cdot\frac{\omega_{pe}^2}{\omega^2}\right) + \frac{\omega_{pi}^2}{\omega^2}$$

$$+ \varepsilon\left[\frac{k_y^2}{k^2}\frac{\omega_{pe}^2}{(\omega-k_z V)^2-\Omega_e^2} + \frac{k_z^2}{k^2}\frac{\omega_{pe}^2}{(\omega-k_z V)^2}\right] \qquad (1)$$

where ω_{pe}, ω_{pi} are the electron, ion plasma frequency, V is the electron drift speed along magnetic field $B_o\hat{z}$, Ω_e is the electron gyrofrequency, and $\varepsilon \equiv n_e/n_o$ is the ratio of the beam density to the total plasma density. Note in Eq. (1) ions are treated as unmagnetized so that $\omega \gg \Omega_i$ and $k_\perp \rho_i \gg 1$ are assumed in accordance with the wave observations in the ACT-1 experiment.

Let us first consider a parallel propagation, $k_y = 0$ and $k_z = k$. Then Eq. (1) is reduced to

$$1 = (1-\varepsilon)\frac{\omega_{pe}^2}{\omega^2} + \frac{\omega_{pi}^2}{\omega^2} + \varepsilon\frac{\omega_{pe}^2}{(\omega-kV)^2} \simeq (1-\varepsilon)\frac{\omega_{pe}^2}{\omega^2} + \varepsilon\frac{\omega_{pe}^2}{(\omega-kV)^2}, \qquad (2)$$

which is a familiar form considered by a number of people.[8,11] It is well-known that a negative energy wave on the beam electrons couples to the positive energy plasma wave at $\omega \tilde{=} \omega_{pe}$ giving rise to an instability. Figure 1 represents the numerical solutions to Eq. (2) for $\varepsilon = 10^{-1}$. For $\omega_{pe}/k \lesssim V$, the instability results from the coupling between a plasma wave $\omega = \omega_{pe}$ and a

beam mode $\omega = kV - \sqrt{\varepsilon}\,\omega_{pe}$, while for $\omega_{pe}/k \gtrsim V$, the instability results from the coupling between two beam modes giving a wave frequency of roughly $\omega = kV$. The maximum growth rate occurs near $kV/\omega_{pe} \approx 1$.[8,11]

For an oblique propagation given by Eq. (1), the ion contribution is still negligible until the propagation is nearly perpendicular to the magnetic field where

$$\frac{k_z^2}{k^2} \lesssim \frac{\omega_{pi}^2}{\omega_{pe}^2} = \frac{m_e}{m_i} \tag{3}$$

is satisfied. For this angle of propagation, it is well-known that the electron plasma waves $\omega = (k_\parallel/k)\omega_{pe}$ go over to the lower hybrid wave $\omega^2 = \omega_{pi}^2/(1+\omega_{pe}^2/\Omega_e^2)$ in the high density limit $\omega_{pi}^2/\Omega_i^2 >> 1$.[12]

Figure 2 shows a typical example for the oblique propagation where the angle θ between $\underline{k}$ and $\underline{B}$ is assumed to be $\theta = 67.5^\circ$. $\varepsilon = 10^{-1}$ and $\Omega_e/\omega_{pe} = \sqrt{2}$ are taken. It is clear that there are two groups of unstable modes. One is associated with the electron plasma wave $\omega \approx (k_\parallel/k)\omega_{pe}$ and the other is associated with the upper hybrid wave destabilized by the beam electrons.[13,14] For small $kV/\omega_{pe} \lesssim 1.5$, electron plasma waves $\omega = (k_\parallel/k)\omega_{pe}$ and $\omega = k_\parallel V - \sqrt{\varepsilon}\,(k_\parallel/k)\omega_{pe}$ are unstable, which are the continuation from the parallel propagation shown in Fig. 1. Both the growth rate and the wave frequency decreases as the propagation becomes more and more perpendicular.

The instability near the upper hybrid resonance frequency, on the other hand, has a larger growth rate as the propagation approaches perpendicular. The instability appears only for a selected band of kV/ω_{pe} as shown in Fig. 2. Note that the cold plasma model used here is valid only for $k_\perp \rho_e << 1$ where $\rho_e = v_t/\Omega_e$ is the electron gyroradius. It is shown that a more accurate treatment of the instability near the electron cyclotron harmonics requires a

kinetic theory which shows a presence of beam-driven instabilities near the harmonics of the electron gyrofrequency, $\omega \sim n\Omega_e$ for $k_\perp \rho_e \sim 1$.[13,14]

III. RESULTS FROM ONE-DIMENSIONAL SIMULATIONS

We shall first describe results obtained from one-dimensional simulations in some detail for different beam densities and velocities relative to the main plasma density and the thermal speed. We shall study the simulation at various angles of propagation with respect to a uniform static magnetic field. The code used is a standard electrostatic one-dimensional model using finite-size particles in a spatial grid. Typically, the simulation length $L = 1024\Delta$ where Δ is the grid size, the number of simulation particles per grid $n = 80\Delta^{-1}$, the initial electron Debye length $\lambda_e = \sqrt{2}\,\Delta$, and the time step of integration $\omega_{pe}\Delta t = 0.2$ are used. $\varepsilon = n_b/n_o$ is varied from 10^{-3} to 0.2 while V/v_t is varied from 3 to 40. Beam temperature in the direction of the magnetic field is assumed to be zero initially while the perpendicular temperature is taken to be equal to v_e. When the beam velocity is much larger than the background thermal speed, $V \gtrsim 10\ v_e$, thermal spread of the beam electrons equal to v_e did not change the simulation results significantly.

Let us first study several cases where the wave propagation is parallel to the magnetic field in which longitudinal motion is completely decoupled from the transverse motion in the electrostatic limit. The first example is $\varepsilon = 0.1$ and $V/v_t = 10$ and the other parameters are defined earlier.

Figure 3 shows the phase-space plots of electrons from the initial condition to the final state. According to the linear theory shown in Fig. 1, the growth rate takes its maximum value near $k \approx \omega_{pe}/V \approx 0.707\Delta^{-1}$ corresponding to the 12th mode of the system. Significant acceleration of

beam electrons as well as the background electrons can be seen at $\omega_{pe}t = 20$ caused by the strong electric field of the unstable modes. Relative amplitude of the electric field energy of the Fourier modes shown in Fig. 4 indicates that at this time there are several dominant modes, modes 12, 14, 15, and 16.

As the instability grows further, trapping of the beam as well as the background electrons is clearly seen in Fig. 3 at $\omega_{pe}t = 30$ where mode 12 and 14 are the most dominant modes. It is interesting to realize that the motion of the trapped particles is roughly symmetric with respect to the wave phase velocity, thereby accelerating a significant fraction of beam and background electrons up to a velocity nearly twice of the original beam velocity.

At $\omega_{pe}t = 50$, significant diffusion in velocity space has taken place associated with the coalescence of the unstable modes shown in Fig. 3, resulting in the smaller amplitude of the electrostatic waves at this time. This diffusion process continues further in time and little evidence for the trapped particle is seen at $\omega_{pe}t = 100$. Nearby complete thermalization has taken place at $\omega_{pe}t = 400$ as shown in Fig. 3. By this time, wave energy is much smaller compared with earlier times when the instability is the strongest as shown in Fig. 4. This is because the waves are absorbed back to the particles via Landau damping associated with the presence of a negative slope of the electron distribution. Note that the simulation results found here are very different from the predictions from a quasilinear theory.[6,7] In particular, note the presence of accelerated beam and background electrons nearly twice the original beam velocity.

Figure 4 indicates the electrostatic field energy of Fourier modes at four different time steps. There are several strongly unstable modes that grow to large amplitudes. At a later time, $\omega_{pe}t = 100$, the energy associated with these modes is reduced to a much smaller amplitude. The particle

distribution has a negative slope for all $v_{\parallel}$ so that it is stable against the plasma instability at this time.

Figure 5 indicates the beam, background, and the total electron distribution at different time steps. The initial distribution shown in (a) spreads in time and, at the same time, the background electrons are accelerated to form a high energy tail. Beam electrons shown in Fig. 5(c), (f) spread to both high and low energies while the average beam velocity decreases in time. The final beam distribution looks triangular, peaking at zero velocity and smoothly extending to nearly twice the initial beam velocity. There is a finite negative slope associated with the beam distribution which is responsible for the damping of the waves after saturation.

The background elections are accelerated to form a high energy tail as a result of trapping as shown in Fig. 5(b), (e). Its final tail distribution is very similar to the beam distribution, suggesting that at the final stage of the simulations, diffusion in velocity space is strong enough to smear out beam and background electrons.

It is interesting to observe that the largest velocity for both beam and background electrons is almost twice the initial beam velocity. This can be explained in the following manner. For a strong instability, such as in this example, the wave energy grows to large amplitude to trap both beam and background electrons. Those trapped electrons oscillate back and forth in the potential well thereby producing a high energy tail. As the amplitude of the unstable waves grow, the trapping width grows and more background particles are trapped. Since the trapping of the background electrons causes the damping of the wave, the instability must saturate when the number of the trapped background electrons approach that of the beam electrons. Since the

motion of a trapped electron is nearly symmetric, the maximum trapping velocity is V in the beam frame which is 2V in the laboratory frame. In reality, however, it should be smaller by a few thermal speeds of the background electrons since the wave amplitude must stop growing when the number of the trapped background electrons approaches the number of beam electrons.

The final total electron distribution shown in Fig. 4(d) confirms the presence of a smooth, finite negative slope $f'(v) < 0$ for $v > 0$ and the presence of a high energy tail. This distribution is stable against plasma instabilities and no changes have been observed during the course of the simulations.

Figure 6 shows the time history and frequency spectrum of two unstable modes, mode 3 where $kV/\omega_{pe} = 0.27$ and mode 12 where $kV/\omega_{pe} = 1$. Mode 3 is a weakly unstable mode and its saturation amplitude is ten times less than that of mode 12. For mode 3, the frequency spectrum shows stable waves at $\omega \simeq \omega_{pe}$, and unstable beam mode at $\omega \simeq kV$. Mode 12 is one of the most unstable modes whose electric field shows amplitude oscillation after reaching the maximum amplitude. The wave energy decreases in time due to the Landau damping associated with the negative slope of the average electron distribution, $f'(v_{\parallel}) < 0$.

The final electron velocity distribution found in the simulation is stable with respect to plasma instabilities since the distribution function is monotonically decreasing with respect to the velocity. The time to develop such a stable distribution is found to be $t \simeq (50 \sim 100)\ \omega_{pe}^{-1}$ which is about 10 e-folding times the most unstable modes. So, on the average, the distance the beam travelled during such a time interval is $Vt \simeq 10^3 \lambda_e$. Such a distance is very short in any experimental device including the ACT-1 so that except for a

narrow region near the beam injection point, one would expect the electron distribution to be given by the final distribution, which has an energetic tail as a result of beam-plasma instability.

Generation of toroidal current in the ACT-1 device via injection of an electron beam may be estimated by calculating the mean-free path of the electrons determined from classical collisions. This is because the current associated with the electrons can only be dissipated by the collisions with the ions as well as with the background electrons when the electron distribution is stable against plasma instabilities.

When the beam density is small compared with the background plasma density, the mean-free path of the beam electrons may be estimated by neglecting collisions between beam electrons and treating the background plasma as a Maxwellian target. Note that the collision time for an electron whose speed is v is proportional to v^3 for $v >> v_e$[15] so that the generation of the high energy tail of the electrons as a result of beam-plasma instabilities could enhance the mean-free path and the generation of toroidal current.

The mean-free path of the electrons may be estimated by $\ell = \langle v_\parallel \tau_e \rangle$ where $\langle\ \rangle$ means averaging over the electron distribution.[5] Here τ_e is the collision time of a beam electron with the background electrons and ions, and is given by, for $v >> v_t$, $\tau_e^{-1} = \tau_{ee}^{-1} + \tau_{ei}^{-1}$ where

$$\tau_{ee} = \frac{1}{2}\tau_{ei} = \frac{m_e^2 v^3}{8\pi n e^4 \ell n\Lambda} \quad . \tag{4}$$

Therefore the mean-free path is given by

$$\ell = \frac{m_e^2}{12\pi n e^4 \ell n\Lambda} \langle v_\parallel v^3 \rangle \propto \langle v_\parallel v^3 \rangle \quad . \tag{5}$$

Similarly, the mean-free path for the current may be given by[5]

$$\ell' = \langle v_\parallel^2 \tau_e \rangle \propto \langle v_\parallel^2 v^3 \rangle \quad . \tag{6}$$

Figure 7 shows the time history of ℓ and ℓ' calculated using the electron distribution found in the simulations as shown by Fig. 5. Both ℓ and ℓ' are normalized by their initial values where a cold beam $\delta(v_\parallel - V)$ is streaming through a Maxwellian background plasma. For short time, $\omega_{pe} t \lesssim 20$, both mean-free paths remain the same as their initial value until they are suddenly reduced by 20% or so at $\omega_{pe} t = 25$. At this time, the unstable waves have grown to large amplitudes so that the beam electrons are decelerated as they give the energy away to the waves. At later times, however, a high energy tail is formed as a result of particle trapping for both beam and background electrons. Such high energy electrons have a long mean-free path as the collision frequency decreases rapidly as v^{-3}. As a result, both ℓ and ℓ' increase in time and their final values are larger than the ones shown in Fig. 7, suggesting that the mean-free path of the electrons and the current generated are more than that of the original beam. In this sense, we may conclude that the beam-plasma instability generates an anomalous conductivity rather than an anomalous resistivity as commonly believed. The simulation results reported here are obtained by using a fixed ion background; however, no appreciable modifications are found by using mobile ions because the ion time scale is much longer than the time scale reported here.

It is of some interest to consider the mean-free path ℓ' defined by Eq. (6) for extreme distributions. For the initial distribution of a cold beam given by

$$f_b(v) = n_b \delta(v_\parallel - V) \quad , \tag{7}$$

$$\ell' \propto \langle v_\parallel^2 v^3 \rangle = \int_o^\infty f_b v_\parallel^5 \, dv_\parallel = n_b V^5 \quad .$$

For a square distribution extending $v_\parallel = 0$ to $v_\parallel = V$, which may be considered an approximation from a quasilinear theory, beam distribution may be given by

$$f_b(v) = \begin{cases} n_b/V & \text{for } 0 < v_\parallel < V \\ 0 & \text{otherwise} \end{cases} \tag{8}$$

so that

$$\ell' \propto \int_o^\infty f_b \, v_\parallel^5 \, dv_\parallel = n_b V^5/6 \quad . \tag{9}$$

Another extreme distribution is to assume a square distribution extending to $v_\parallel = 2V$ from $v_\parallel = 0$ so that

$$f_b(v) = \begin{cases} n_b/2V & \text{for } 0 < v_\parallel < 2V \\ 0 & \text{otherwise} \end{cases} \quad , \tag{10}$$

$$\ell' \propto \int_o^\infty f_b v^5 dv = (16/3) n_b V^5 \quad . \tag{11}$$

It is clear that the mean-free path ℓ' calculated from a distribution similar to the one found in the quasilinear theory, gives a grossly underestimated value because of the neglect of the high energy tail. The other distribution given by Eq. (10), which has a flat tail extending to 2V, overestimates the mean-free path because the tail population is higher than the distribution found in the simulation results.

The experimental results obtained from ACT-1[5] do not show the toroidal current as much as the simulation, although it is certainly much larger than the estimate given from the quasilinear estimate of Eq. (9). The ACT-1 results, however, show closer agreement with the two-dimensional results given in Sec. V, suggesting that a pure one-dimensional model which assumes a presence of beam electrons with an infinite transverse dimension overestimates the enhancement of the high energy electrons.

In an actual experiment such as done in the ACT-1, the beam dimension, d, is finite and is only 100 λ_e or so, and therefore the unstable plasma waves propagate obliquely to the magnetic field. In this case, the plasma instabilities are expected to be weaker (as seen in the linear dispersion relation shown in Fig. 2) so that the enhancement of high energy electrons becomes smaller.

When the beam transverse dimension is large enough so that d is much larger than the wavelength of the most unstable mode of the beam plasma instability, $k^{-1} \approx V/\omega_{pe}$, the results of the one-dimensional simulation should remain valid because the most unstable modes are nearly one-dimensional. This condition is given by

$$d >> 2\pi V/\omega_{pe} \quad . \tag{12}$$

We have run another simulation in which all the simulation parameters were kept the same, except that the initial beam temperature is assumed equal to that of the background electrons. No significant changes were found and the results found for the cold beam electrons remain valid.

We shall now study the results of simulation where the relative beam density has been changed. When the beam density is increased to $\varepsilon = 0.2$, the

qualitative characteristics of the instability remain the same except for the enhanced tail population and hence the mean-free path of beam propagation.

Figure 8 shows the total (a), background (b), and beam electron distribution (c), at t = 0 and $\omega_{pe}t$ = 400, well after the saturation of the instability. The high energy tail extends to almost 2V and there is a smooth negative slope of the total distribution which may be responsible for the absorption of the lower hybrid wave used to drive a current in a tokamak.[5] Clearly, the final distribution Landau damps waves excited by the beam-plasma instability so that the wave amplitude is near the noise level at the end of the simulation.

Figure 8(d), (e) shows the relative mean-free path ℓ and ℓ' normalized by their initial values. In this case, the mean-free path for the current is more than twice the mean-free path associated with the initial cold beam.

The enhancement of the high energy electrons and hence the mean-free path of the current decreases as the beam density is reduced while keeping the beam velocity constant at V/v_t = 10. As the beam density is reduced, the instability saturates at a low level thereby generating a smaller population of trapped electrons. The particle distribution approaches that predicted from the quasilinear theory in the long time scale after the coherent phase-space structure associated with particle trapping is smeared out.

Figure 9 shows the initial and final particle distributions at $\omega_{pe}t$ = 400 and the associated mean-free paths for ε = 0.05. Note the changes of the particle distribution where the maximum velocity of high energy particles is 1.6V, significantly less than 2V. Also, the slope of the distribution for v < V is much smaller while for v > V it is still finite, giving rise to the enhanced current generation. The relative mean-free paths are still larger than 1 at the end of the simulations. However, the gain is decreasing as the

beam density is reduced relative to the background density as shown in Fig. 9(d), (e).

When the beam density is reduced to 1% as shown in Fig. 10, the final distribution approaches further to that predicted from a quasilinear theory, although there are still clear signs of energetic electrons generated from both the beam and main electrons. The mean-free path finally becomes less than 1, meaning that the toroidal current generated will be less than that associated with the initial cold beam.

When the beam density is further reduced to 0.1% as shown in Fig. 11, coherent particle trapping is seen at $\omega_{pe}t = 100$, coalesces gradually at $\omega_{pe}t = 200$, and then gives rise to a smooth phase-space distribution at $\omega_{pe}t = 400$, whose velocity distribution is nearly flat for $v < V$ with a small number of high energy particles. In this case, the final relative mean-free path for the current ℓ', is about 0.66 of the initial value, which is much smaller than the mean-free path calculated from the initial cold beam.

The next example is the case where the beam velocity is doubled to $V = 20v_e$ while the beam density is kept at $\varepsilon = 0.1$. This case is intended to study if the final electron distribution is significantly different from the previous $V = 10v_t$ case. The most unstable mode in this case is approximately the 7th mode of the system. As in the case of $V = 10v_t$, several unstable modes grow to large amplitude. The final particle distribution shown in Fig. 12 at $\omega_{pe}t = 400$ remains almost the same with the high energy tail extending to 2V. The shape of the tail distribution is roughly the same for the beam and main electrons as a result of strong trapping accompanied by a mixing in phase space. Again the relative mean-free path shown in Fig. 12(d), (e) is significantly larger than 1 and numerically almost the same as the case where $V = 10v_t$.

Similar tail distribution is found for even a larger beam velocity. It is found that the final distribution at $\omega_{pe}t = 400$ for $V = 40\ v_t$ is initially similar again to those found for $V = 10\ V_t$ and $20\ V_t$, suggesting a similar solution for the high energy tail. Relative mean-free path therefore stays about the same.

Reducing the beam velocity gives qualitatively the same results even though the instability is much weaker. Figure 13 shows the particle distribution for $V = 3\ v_t$ initially for $\varepsilon = 0.1$. Both the beam and the background electrons are accelerated to form a high energy tail. The relative mean-free path is larger than 1 although the enhancement factor is small because the instability is much weaker as shown in Fig. 13(d), (e).

We shall now consider an example of one-dimensional simulation where the unstable waves propagate obliquely with respect to the external magnetic field. As mentioned earlier, wave propagation in an experimental device cannot be strictly along the magnetic field ($\underset{\sim}{k} \times \underset{\sim}{B}_o \neq 0$) due to the finite dimension of the electron beam. The example considered is $\varepsilon = 0.1$, $V = 10v_t$, and $\theta = 67.5°$ where θ is the angle between $\underset{\sim}{k}$ and $\underset{\sim}{B}_o$. The dispersion relation, given by Fig. 2, reveals that the oblique plasma wave $\omega = (k_\parallel/k)\ \omega_{pe}$ and the beam mode $\omega = k_\parallel V$ remain unstable for $kV/\omega_{pe} \gtrsim 1$ in addition to the instability near the upper hybrid frequency for large kV/ω_{pe}.

Figure 14 shows the initial and final electron distribution along magnetic field, $f(v_\parallel)$, averaged over $v_\perp$ at $t = 0$ and $\omega_{pe}t = 400$. Again both the beam and background electrons form a high energy tail with a presence of finite negative slope very similar to the case of parallel propagation. Frequency analysis reveals that the dominant modes are the electron plasma waves propagating obliquely to the magnetic field for modes 6-15 which reach large amplitude. In addition, smaller peaks in the frequency spectrum are seen near $\omega = \omega_{UH} = (\omega_{pe}^2 + \Omega_e^2)^{1/2}$, which are also predicted.

Again the relative mean-free path shown in Fig. 14(d), (e) is enhanced above the initial value although the enhancement is modest compared with the parallel propagation. This is because the instability is weaker in the case of oblique propagation resulting in the smaller acceleration of high energy particles. Also the initial beam energy is partly fed to the perpendicular heating.

Because of the presence of perpendicular electric field $E_\perp$, heating of electrons perpendicular to the magnetic field takes place as shown in Fig. 15. Both the beam and background electrons are heated to the same degree. However, the perpendicular heating remains much smaller than the parallel heating in this example. We shall now discuss results obtained from a two-dimensional model and compare them with one-dimensional results.

IV. RESULTS FROM TWO-DIMENSIONAL SIMULATIONS

The two-dimensional model used is an electrostatic code with periodic boundary conditions in both x,y directions. The external magnetic field is in the x-y plane pointing to y-direction $\underset{\sim}{B}_o\hat{y}$. A 128 × 128 grid was used with 9 ~ 16 electrons per square grid. $\lambda_e = \Delta$ and $\Omega_e/\omega_{pe} = 1.2$ are taken. Ions are assumed to form a uniform background although calculations including mobile ions are also performed to study the effects of ions. In order to simulate a finite dimension of an electron beam in a uniform periodic simulation, Fourier modes of the electrostatic field having only $k_\parallel = k_y$ are deleted in the numerical simulations. This is done by assuming $\underset{\sim}{E}(k_x = 0, k_y) = 0$ for one-dimensional modes propagating along the magnetic field. This model appears better than actually modeling a beam of finite transverse dimension since the simulation plasma is only 128 - Debye lengths wide. The size of the electron beam used in the ACT-1 is about the same as the simulation model.

The parameters for the first example of the two-dimensional simulation are $\lambda_e = \Delta$, $v = 10\ v_t$, $\varepsilon = 0.1$, and $\Omega_e/\omega_{pe} = 1.2$. Note the system is only 128 - Debye lengths along the magnetic field so that the most unstable mode associated with the oblique electron waves is the second longest wavelength mode in the system. Figure 16 shows the electrostatic potential contours at $\omega_{pe}t$ = 30, 50, and 250. At early time, $\omega_{pe}t$ = 30, the most unstable mode, $(k_x, k_y) = (2\pi L)^{-1}(m,n) = (2\pi/L)^{-1}(1,2)$ shows clear dominance in the structure of the potential contour. At later time, $\omega_{pe}t$ = 50, several other modes (m,n) = (1,1), (2,2), and (2,1) grow to large amplitude. Eventually, the longest mode (m,n) = (1,1) survives, which is dissipated showly via Landau damping.

The corresponding phase-space plots averaged near x and $v_\perp$ ($v_\parallel$) = (y, v_y) are shown in Fig. 17. Coherent structure in phase space caused by the (m,n) = (1,2) mode at $\omega_{pe}t$ = 30 is phase-mixed later, $\omega_{pe}t$ = 50 is associated with the growth of several other modes and eventually shows little evidence of coherent particle trapping at $\omega_{pe}t$ = 250. It appears that the phase mixing proceeds much faster in two dimensions than in one dimension. This is because the degree of freedom for particle motion is increased in two dimensions.

Figures 18 and 19 show the velocity distribution for parallel and perpendicular (v_z) components with respect to the magnetic field at $\omega_{pe}t$ = 250 when the instability has been thermalized. Both the beam and main electrons form a high energy tail and the total distribution shows a negative slope in good agreement with one-dimensional simulations. The maximum velocity of the tail particles is 1.5V which is somewhat smaller than that found for parallel propagation ($\underset{\sim}{k} \times \underset{\sim}{B}_o = 0$) but is closer to the results found for the oblique propagation. Perpendicular velocity distribution shown in Fig. 19 shows a comparable heating for both beam and background electrons which is also in close agreement with the one-dimensional results for oblique propagation.

Relative mean-free path for this case shown in Fig. 18 (d), (e) for ℓ and ℓ' remains near unity after the instability is thermalized. This is consistent with the relatively modest acceleration of high energy particles and also agrees well with the ACT-1 observations.[5] Since the beam dimension, L_x, is about the same as the parallel wavelength of the unstable modes, it is clear that the one-dimensional results for parallel propagation ($\underset{\sim}{k} \times \underset{\sim}{B}_o \approx 0$) overestimate the population of the high energy tail, thereby making the relative mean-free path longer than the one found here.

Frequency analysis of the Fourier modes of the electrostatic potential confirms that for long wavelengths, which are the dominant modes in this simulation, the frequency peaks near the oblique plasma wave $\omega = (k_\parallel/k)\omega_{pe}$ and much less energy is found at the upper hybrid frequency. For shorter wavelengths, more and more field energy is found near the upper hybrid and higher frequencies although their amplitude remains small compared with the long wavelength modes.

Two-dimensional simulations using a higher drift velocity, $V = 20v_t$, while keeping the other simulation parameters the same show a much more perpendicular heating while the high energy tail along the magnetic field is substantially reduced compared with the results found for the $V = 10\ v_t$ case. This is because of the fact that the simulation system is not long enough to support all the dominant modes for such a high drift velocity of the electron beam. Large fractions of beam energy therefore went to the perpendicular modes resulting in enhanced perpendicular heating in this case.

For a smaller drift velocity, $V = 3\ v_t$, simulation results show a velocity distribution similar to the one-dimensional simulations given by Fig. 13 with a small high energy tail. In this case, one-dimensional results should be a good approximation to the two-dimensional model since the parallel

wavelength of the most unstable mode $k_{\parallel}^{-1} \approx 2\pi v/\omega_{pe}$ is much smaller than the beam dimension. Therefore, the condition given by Eq. (12) is well satisfied.

Since the two-dimensional simulations include modes which propagate nearly perpendicular to the magnetic field, $k_{\parallel}/k \lesssim (m_e/m_i)^{1/2}$, the ion response cannot be neglected for such propagation. Simulations with mobile ions confirm the presence of lower hybrid waves near $\omega \approx \omega_{pi}$ for such oblique propagations and small ion perpendicular heating has been observed. The effects on the electrons caused by such ion waves, however, remain small and no significant modifications are found compared with the two-dimensional model with the immobile ion background. This is because the electron plasma, upper hybrid, and electron cyclotron harmonic waves play a key role in determining the electron dynamics.

V. CONCLUSIONS

We have shown that the current drive experiment via injection of an electron beam in the ACT-1 can be well explained by using the results obtained from nonlinear plasma simulations. In particular, generation of a high energy tail, the presence of a smooth, negative slope of the particle distribution function along the magnetic field, and the mean-free path of the electrons show good agreement between experimental observations and numerical simulations. The fact that the mean-free path of the beam propagation is much longer than what one would expect from a quasilinear theory may be important not only for current drive in a toroidal device but also for other applications, such as beam propagation in space. While the mean-free path was estimated by using a test particle slowing down time, we plan to solve full Fokker-Planck equations using the electron distribution found in the simulations. While the simulations are carried out using periodic boundary

conditions, it is possible to use a nonperiodic system to study convective instabilities.[10,16] These results will be reported in the near future.

ACKNOWLEDGMENTS

This work was supported by the United States Department of Energy Contract No. DE-AC02-76-CHO-3073. In addition, one of the authors (HO) acknowledges support from National Science Foundation Grant ATM-83-11102.

REFERENCES

1 A. Mohri, Phys. Rev. Lett. 34, 574 (1975).

2 N. J. Fisch, Phys. Rev. Lett. 41, 873 (1978).

3 S. Bernabei, C. Daughney, P. Efthimion, W. Hooke, J. Hosea, F. Jobes, A. Martin, E. Mazzucato, E. Meservey, R. Motley, J. Stevens, S. von Goeler, and R. Wilson, Phys. Rev. Lett. 49, 1255 (1982).

4 J. M. Dawson and P. K. Kaw, Phys. Rev. Lett. 48, 1730 (1981).

5 R. Horton, Lower Hybrid Current Drive in Electron-Beam Plasma, Ph.D dissertation, Astrophysical Sciences Department, Princeton University, 1985.

6 B. B. Kadomtsev, Plasma Turbulence, (Academic Press, NY, 1985) p. 15.

7 W. E. Drummond and D. Pines, Nucl. Fusion, Suppl. Pt 3, 1049 (1962).

8 T. M. O'Neil, J. H. Winfrey, and J. H. Malberg, Phys. Fluids 14, 1204 (1971).

9 K. V. Roberts and H. L. Berk, Phys. Rev. Lett. 19, 297 (1967).

10 A. T. Lin and J. E. Rowe, Phys. Fluids 15, 166 (1972).

11 S. Kainer, J. Dawson, R. Shanny, and T. Coffey, Phys. Fluids 3, 493 (1972).

12 J. M. McBride, E. Ott, J. P. Boris, and J. H. Orens, Phys. Fluids 15, 2367 (1972).

13 M. Seidel, Phys. Fluids 13, 966 (1970).

14 K. Mizuno and M. Tanaka, Phys. Fluids 17, 156 (1974).

15 D. V. Sivukkin, Reviews of Plasma Physics Vol. 4, ed. by M. A. Leontovich (Consultants Bureau, NY, 1966) P. 142.

16 H. Okuda and M. Ashour-Abdalla, J. Geophys. Res. 88, 899 (1983).

FIGURE CAPTIONS

FIG. 1. Solution to the dispersion relation, Eq. (2) for the parallel propagation. $\varepsilon = 0.1$ is assumed. Note a stable root near $\omega = -\omega_{pe}$ is not shown here.

FIG. 2. Plot of the unstable roots from the dispersion relation, Eq. (1), for the oblique propagation. $\varepsilon = 0.1$, $\Omega_e/\omega_{pe} = \sqrt{2}$, and $\theta = 67.5^{\circ}$ are assumed where θ is the angle between $\underset{\sim}{k}$ and $\underset{\sim}{B}_0$.

FIG. 3. Phase-space plots for the beam-plasma instability. $\varepsilon = 0.1$, $V = 10\ v_t$, $\theta = 0$, and $L = 1024\Delta$ are chosen. Note the generation of high energy electrons as a result of particle trapping.

FIG. 4. Relative amplitude of the electrostatic field energy for each Fourier mode at four different times.

FIG. 5. Electron distribution functions for the total, beam, and background electrons. Initial distribution (a), background and beam distribution at $\omega_{pe}t = 30$ (b), (c). Final total (d), background (e), and beam (f) distribution at $\omega_{pe}t = 400$.

FIG. 6. Time history of the electric field of two Fourier modes, mode 3 and mode 11, and their frequency spectrum. Only the relative amplitude is shown.

FIG. 7. Mean-free paths ℓ and ℓ' of the electrons and current defined by Eqs. (5) and (6) in the text normalized by the mean-free paths for the initial cold beam.

FIG. 8. Initial and final total (a), background (b), and beam (c) electron distributions and the relative mean-free paths ℓ(d) and ℓ'(e) for ε = 0.2 and V = 10 v_t.

FIG. 9. Initial and final total (a), background (b), and beam (c) particle distributions and the relative mean-free paths ℓ(d), ℓ'(e) for ε = 0.05 and V = 10 v_t.

FIG. 10. Initial and final total (a), background (b), and beam (c) electron distributions and the relative mean-free path ℓ(d), ℓ'(e) for ε = 0.01 and V = 10 v_t.

FIG. 11. Phase- space plots at $\omega_{pe}t$ = 100 (a), 200 (b), and 400 (c); and the final electron distributions for total (d), background (e), and beam electrons (f) for ε = 0.001 and V = 10 v_t.

FIG. 12. Initial and final total (a), background (b), and beam (c) electron distributions and the relative mean-free path ℓ(d), ℓ'(e) for ε = 0.1 and V = 20 v_t.

FIG. 13. Initial and final total (a), background (b), and beam (c) electron distribution and the relative mean free path ℓ(d) and ℓ'(e) for ε = 0.1 and V = 3v_t.

FIG. 14. Initial and final total (a), background (b), and beam (c) electron distributions along the magnetic field averaged over the perpendicular velocities for an oblique propagation and the relative mean-free path ℓ (d), ℓ'(e). $\varepsilon = 0.1$, $V = 10\ v_t$, $\Omega_e/\omega_{pe} = \sqrt{2}$, and $\theta = 67.5°$ are assumed.

FIG. 15. Initial and final total (a), background (b), and beam (c) electron perpendicular velocity distribution, $f(v_z)$, averaged over v_x and v_y. $f(v_x)$ is almost the same to $f(v_z)$. $\varepsilon = 0.1$, $V = 10 v_t$, $\Omega_e = \sqrt{2}\ \omega_{pe}$, and $\theta = 67.5°$

FIG. 16. Contour plot for the electrostatic potential for a two-dimensional simulation at $\omega_{pe}t = 30$, 50, and 250. $128\ \lambda e \times 128 \lambda e$, $\varepsilon = 0.1$, $V = 10\ v_e$, and $\Omega_e = 1.2\ \omega_{pe}$. A $128\ \lambda_e \times 128\ \lambda_e$ grid is used.

FIG. 17. Phase-space plot $y - v_\parallel$ at $\omega_{pe}t = 30$, 50, and 250 for a two-dimensional simulation. $\varepsilon = 0.1$, $V = 10\ v_e$, and $\Omega_e = 1.2\ \omega_{pe}$.

FIG. 18. Initial and final electron distributions along the magnetic field averaged over perpendicular velocities for total (a), background (b), and beam (c) electrons and the relative mean-free path ℓ (d) and ℓ'(e) for a two-dimensional simulation. $\varepsilon = 0.1$, $V = 10\ v_e$, and $\Omega_e = 1.2\ \omega_{pe}$.

FIG. 19. Initial and final total (a), background (b), and beam (c) electron perpendicular velocity distribution, $f(v_z)$ averaged over v_x and v_y for a two-dimensional simulation. $f(v_x)$ is very similar to $f(v_z)$. $\varepsilon = 0.1$, $V = 10\ v_e$, and $\Omega_{ce} = 1.2\ \omega_{pe}$.

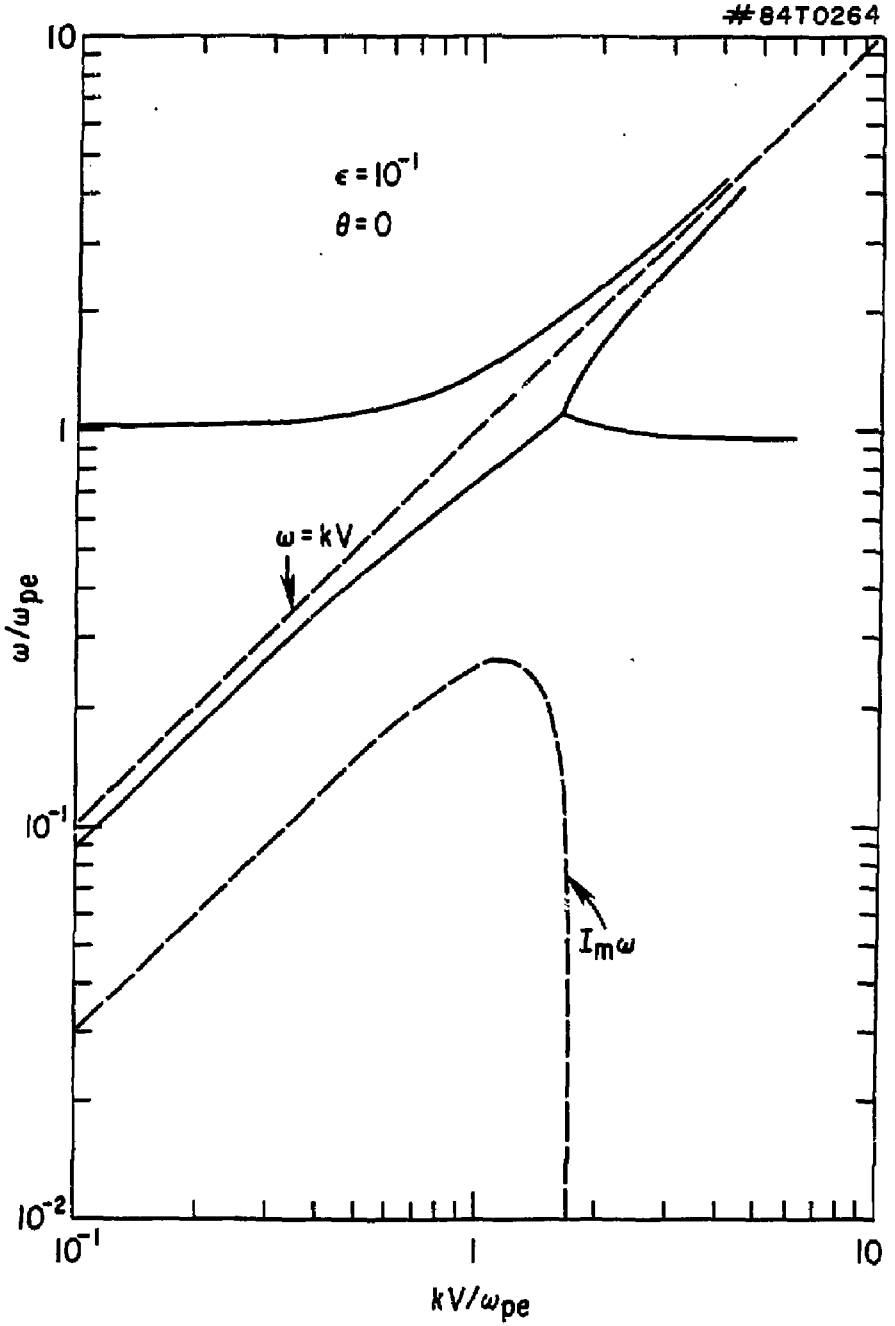
#84T0264
10
1
10^{-1}
10^{-2}
$\epsilon = 10^{-1}$
$\theta = 0$
$\omega = kV$
$I_m\omega$
ω/ω_{pe}
kV/ω_{pe}
10^{-1}
1
10

Fig. 1

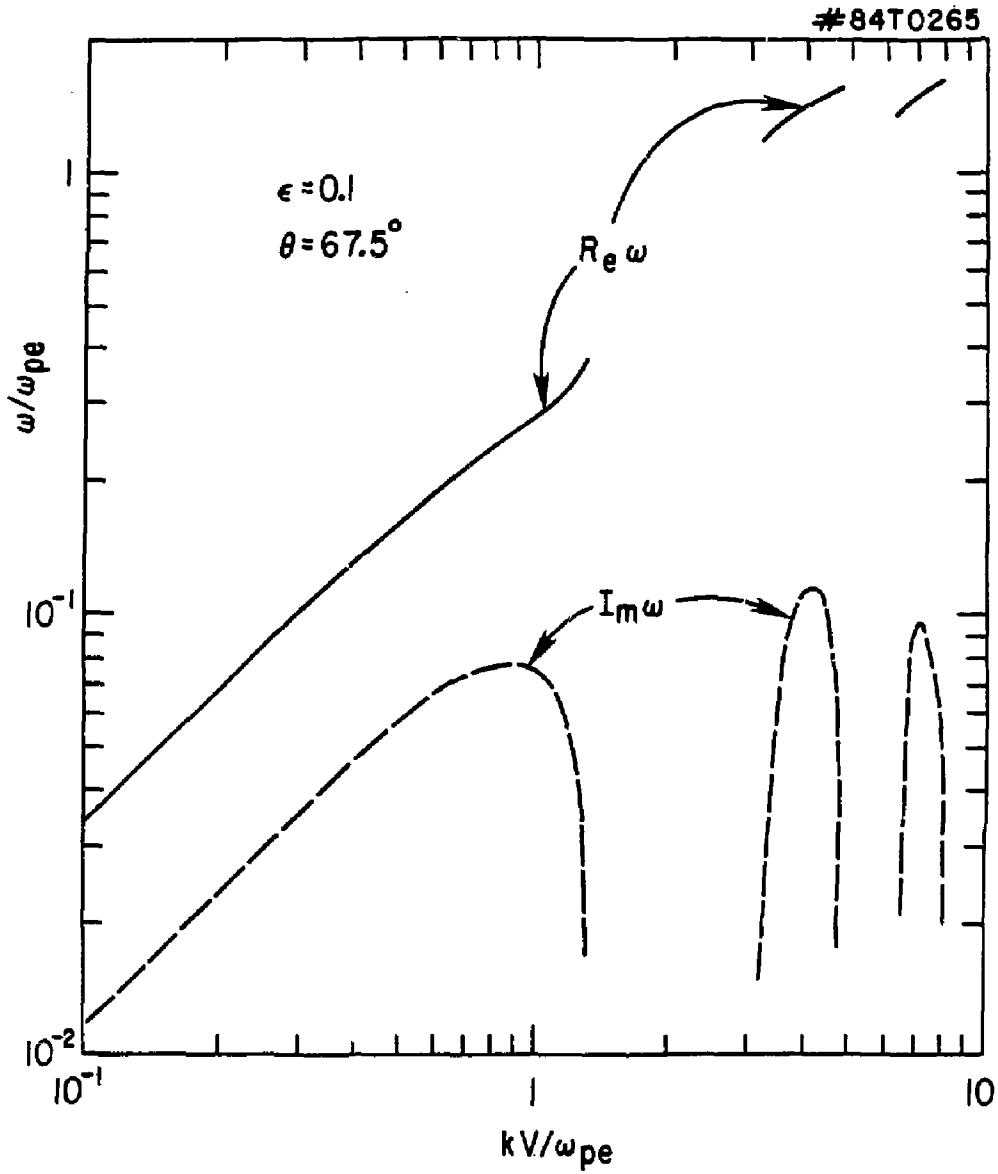

Fig. 2

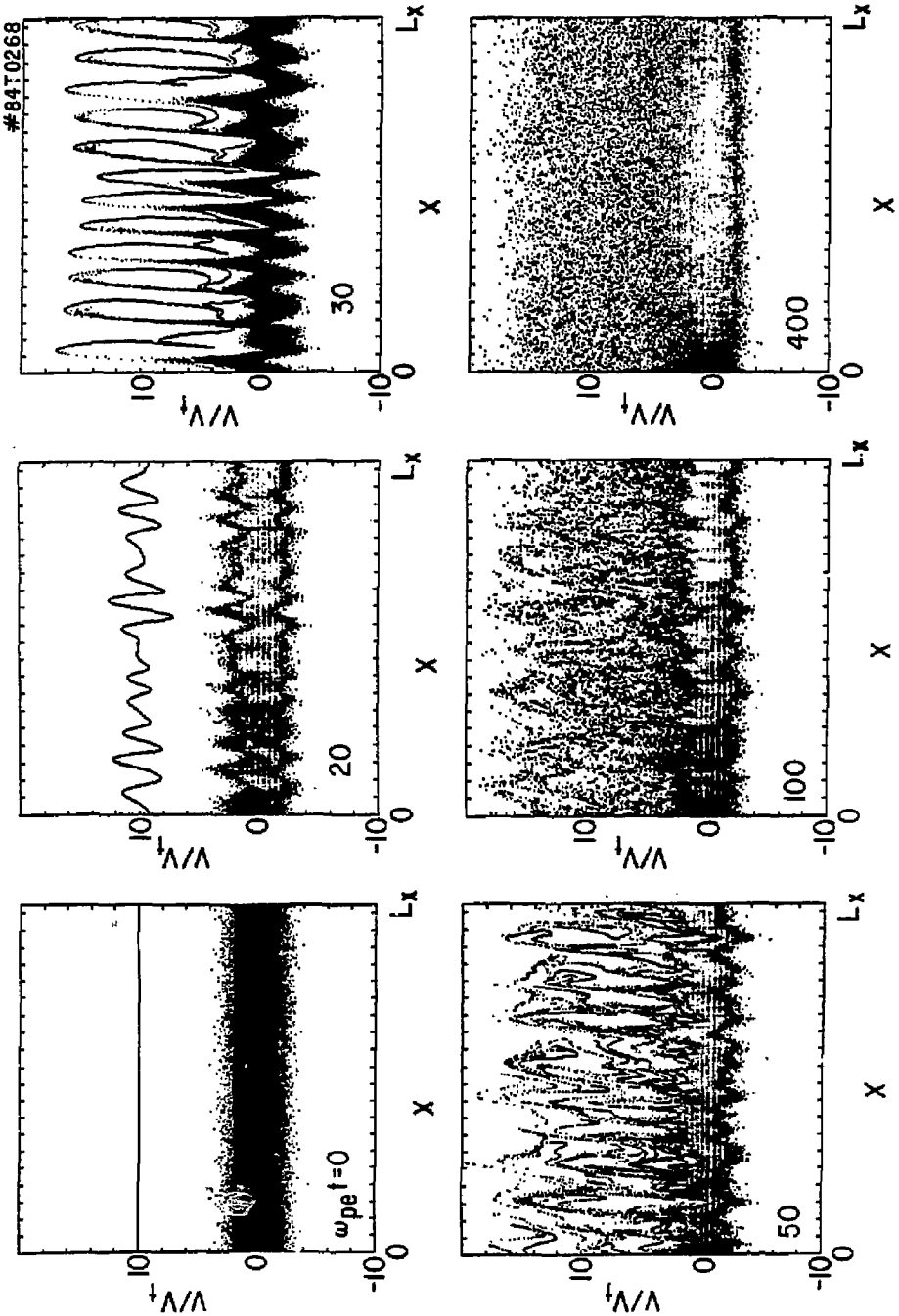

Fig. 3

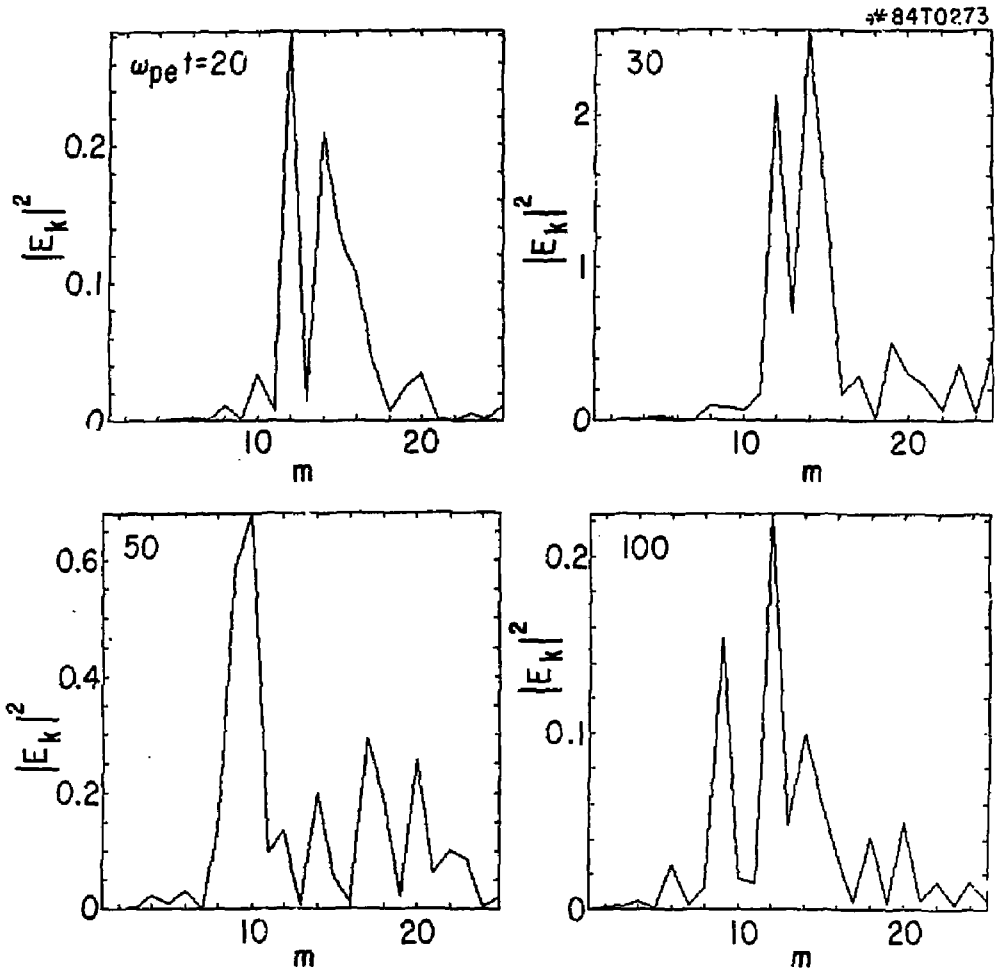

Fig. 4

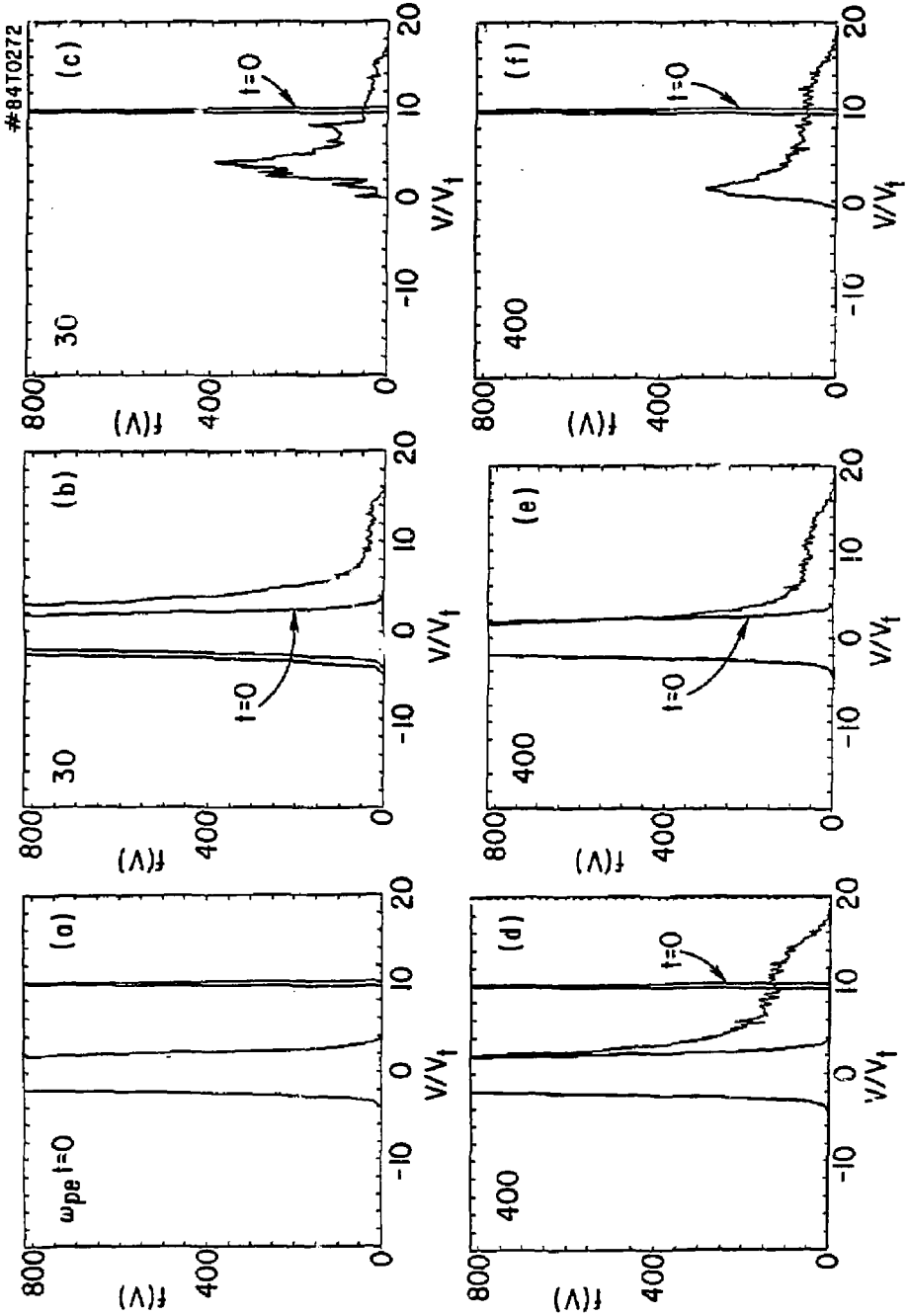
#84T0272
(a)
ω_{pe} t=0
(b)
30
t=0
(c)
30
t=0
(d)
400
t=0
(e)
400
t=0
(f)
400
t=0
f(V)
800
400
0
V/V$_t$
20
10
0
-10

Fig. 5

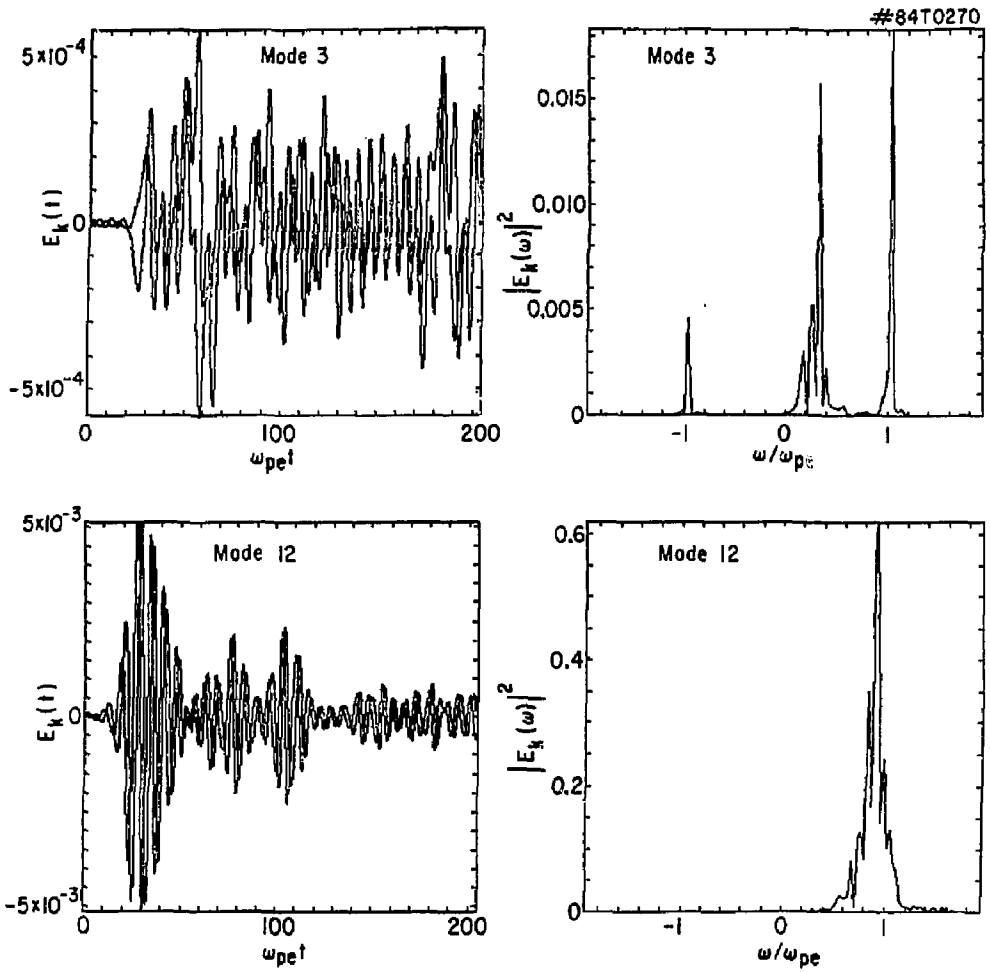
#84T0270
Mode 3
Mode 3
Mode 12
Mode 12
$E_k(t)$
$|E_k(\omega)|^2$
$\omega_{pe}t$
ω/ω_{pe}
5x10^{-4}
-5x10^{-4}
5x10^{-3}
-5x10^{-3}
0
100
200
0.015
0.010
0.005
0.6
0.4
0.2
-1
1

Fig. 6

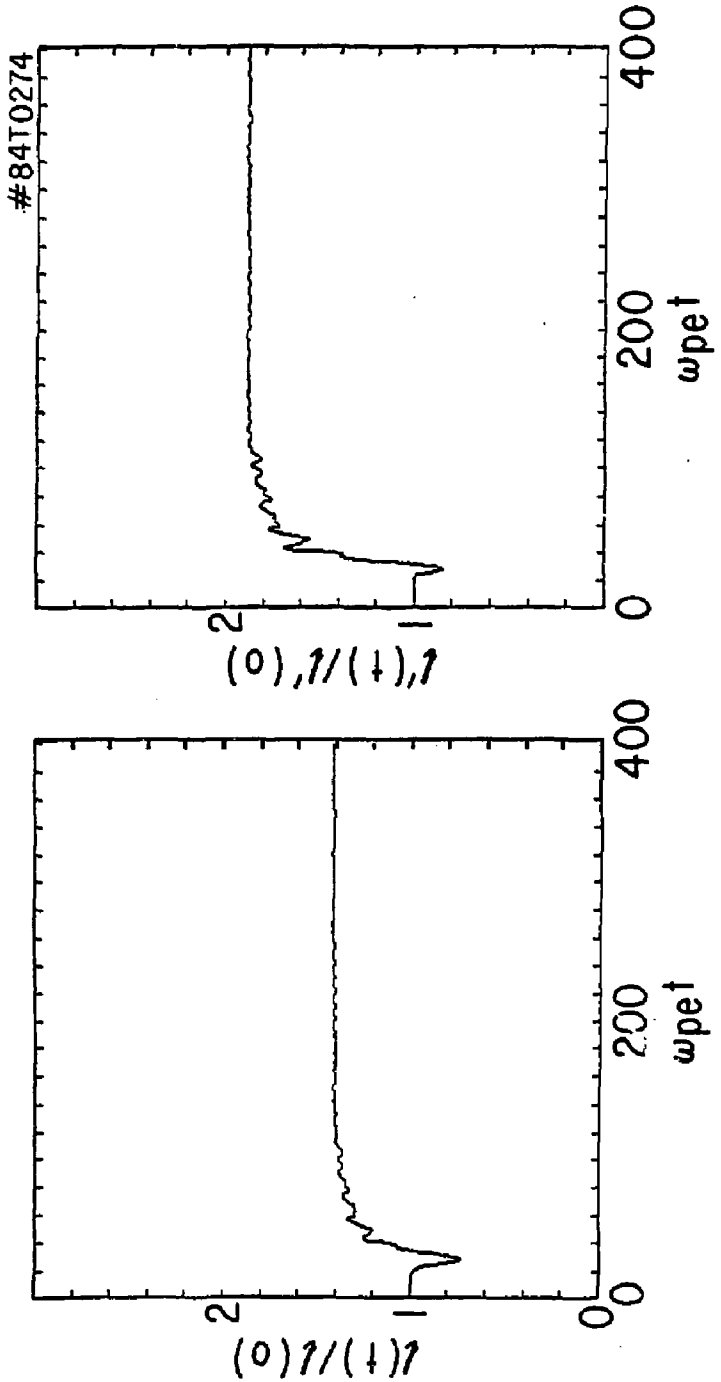

Fig. 7

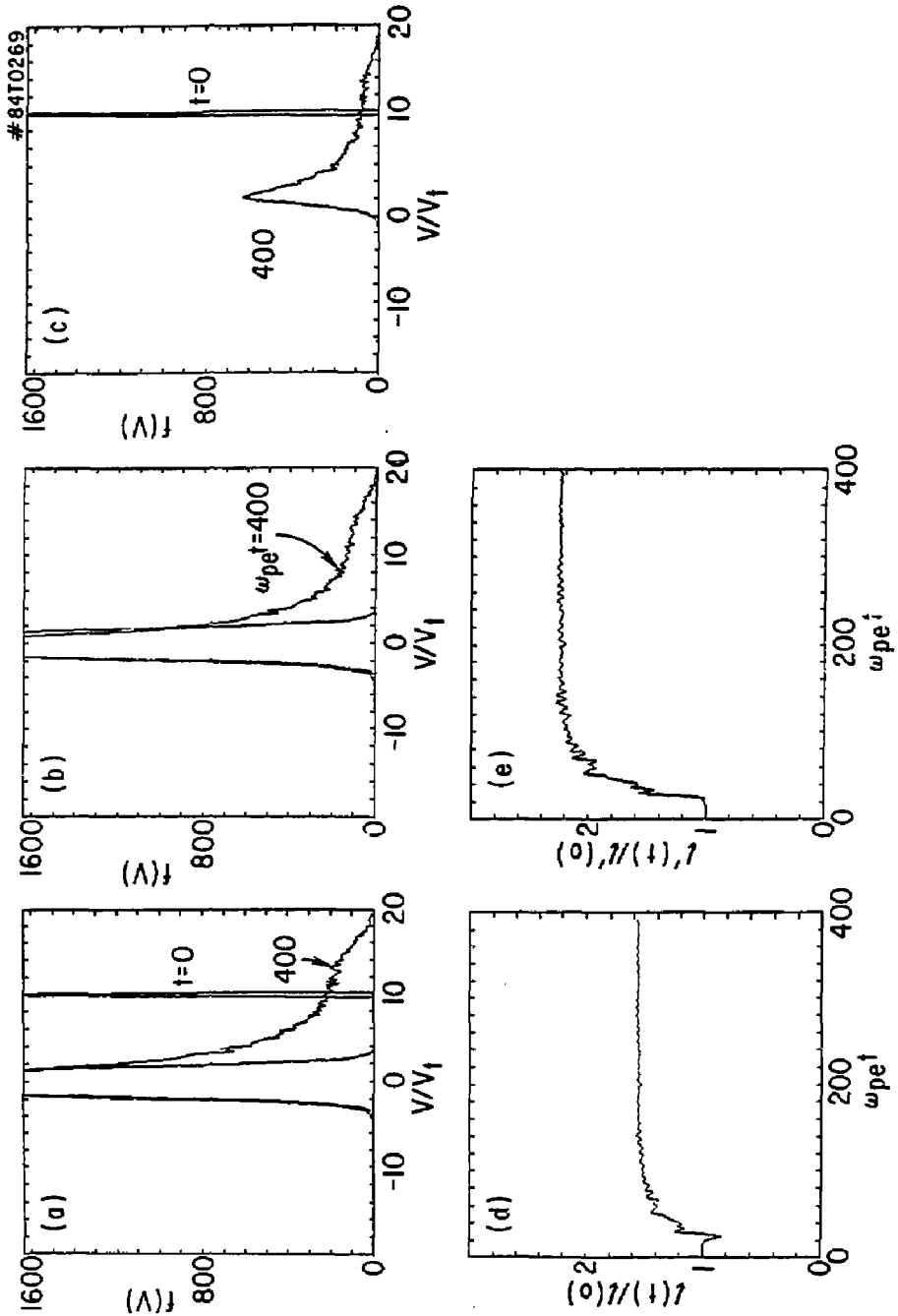

Fig. 8

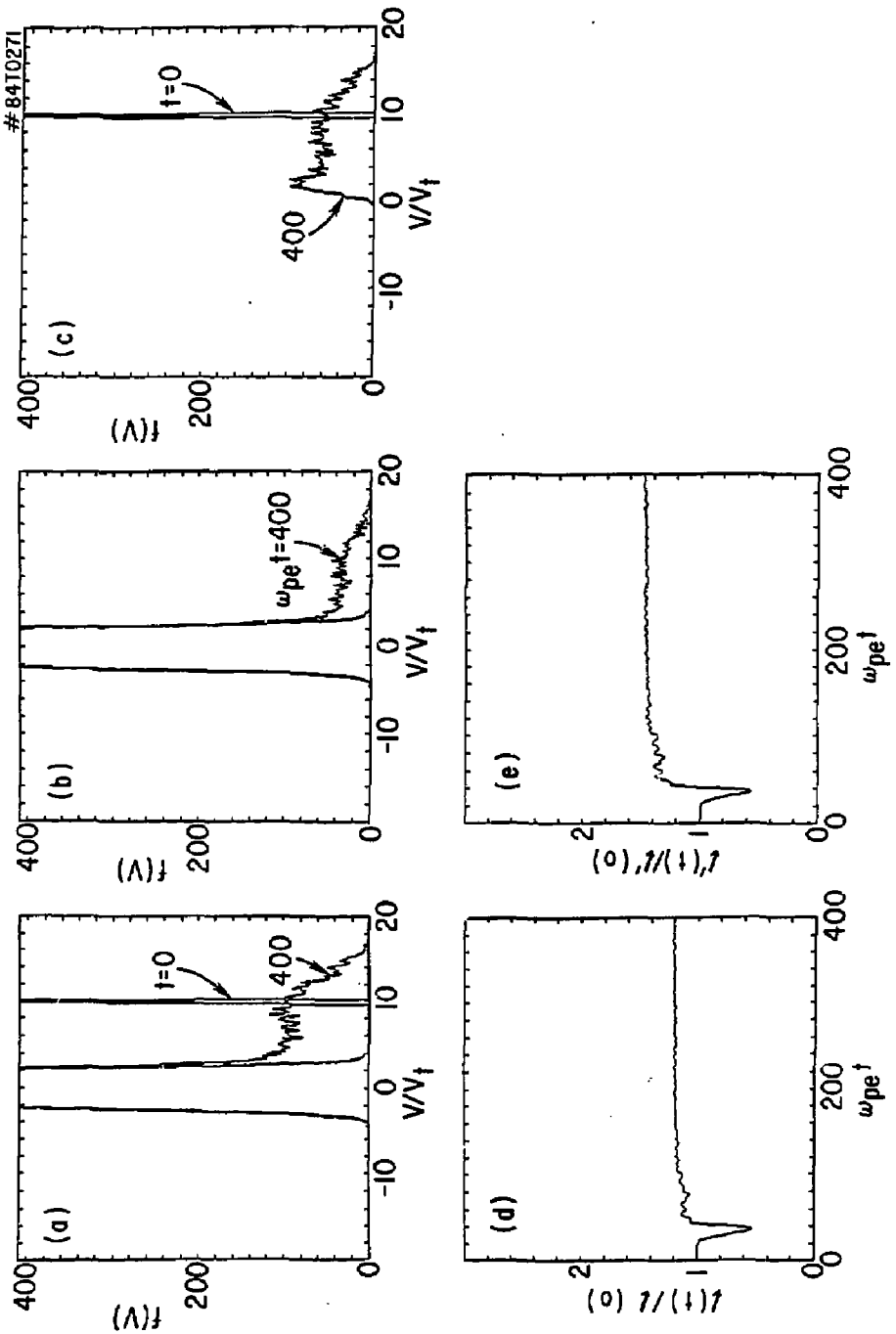

Fig. 9

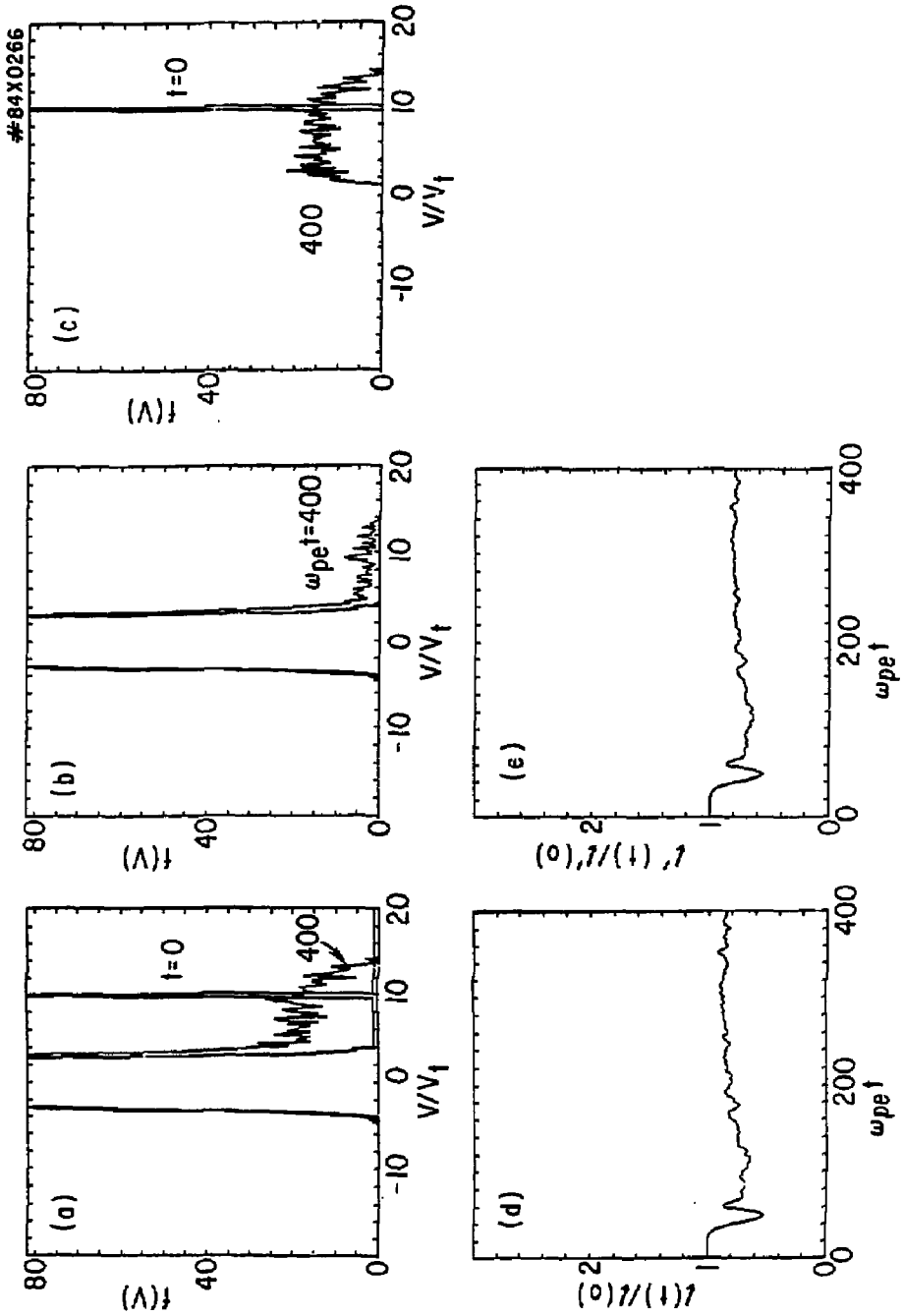

Fig. 10

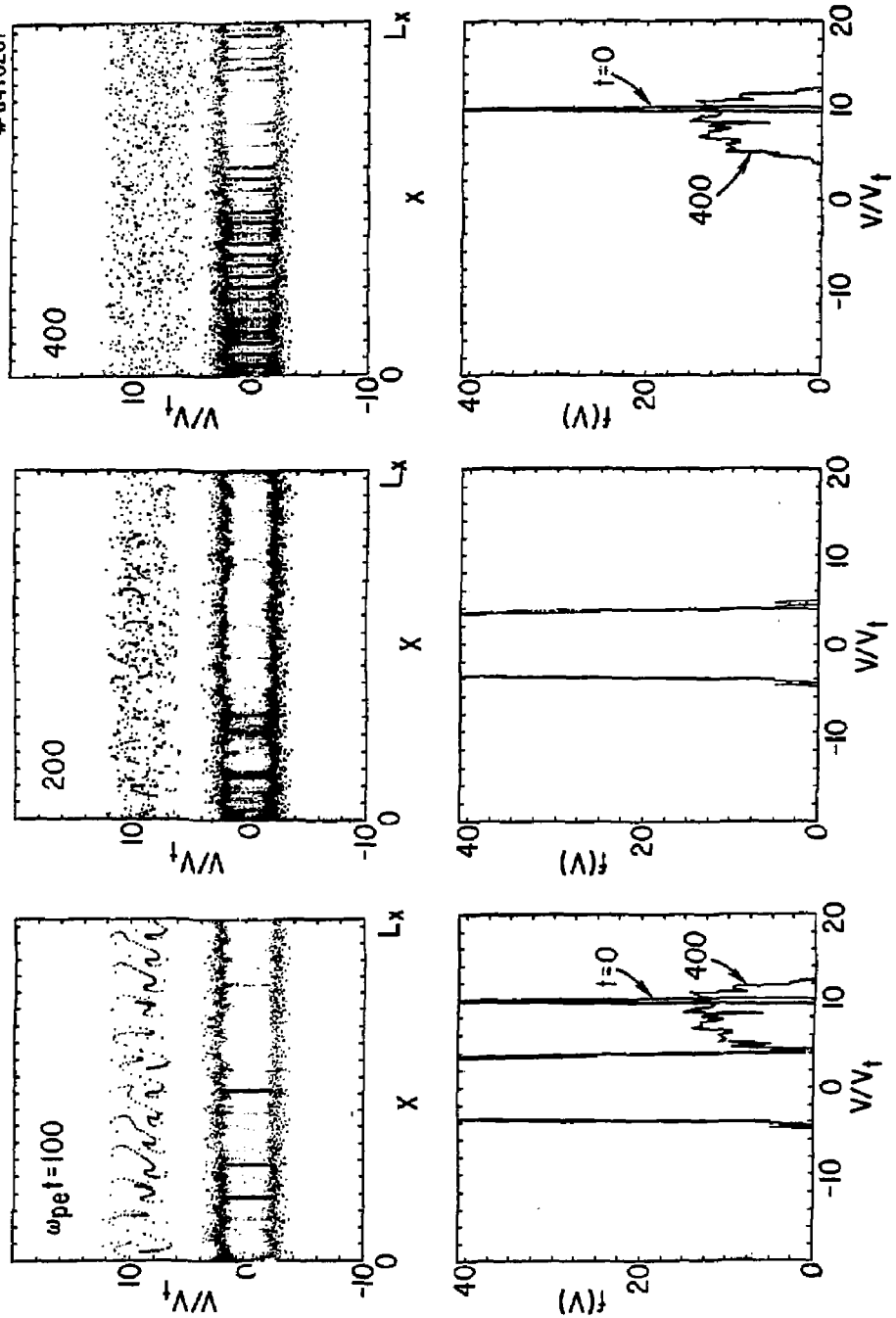

Fig. 11

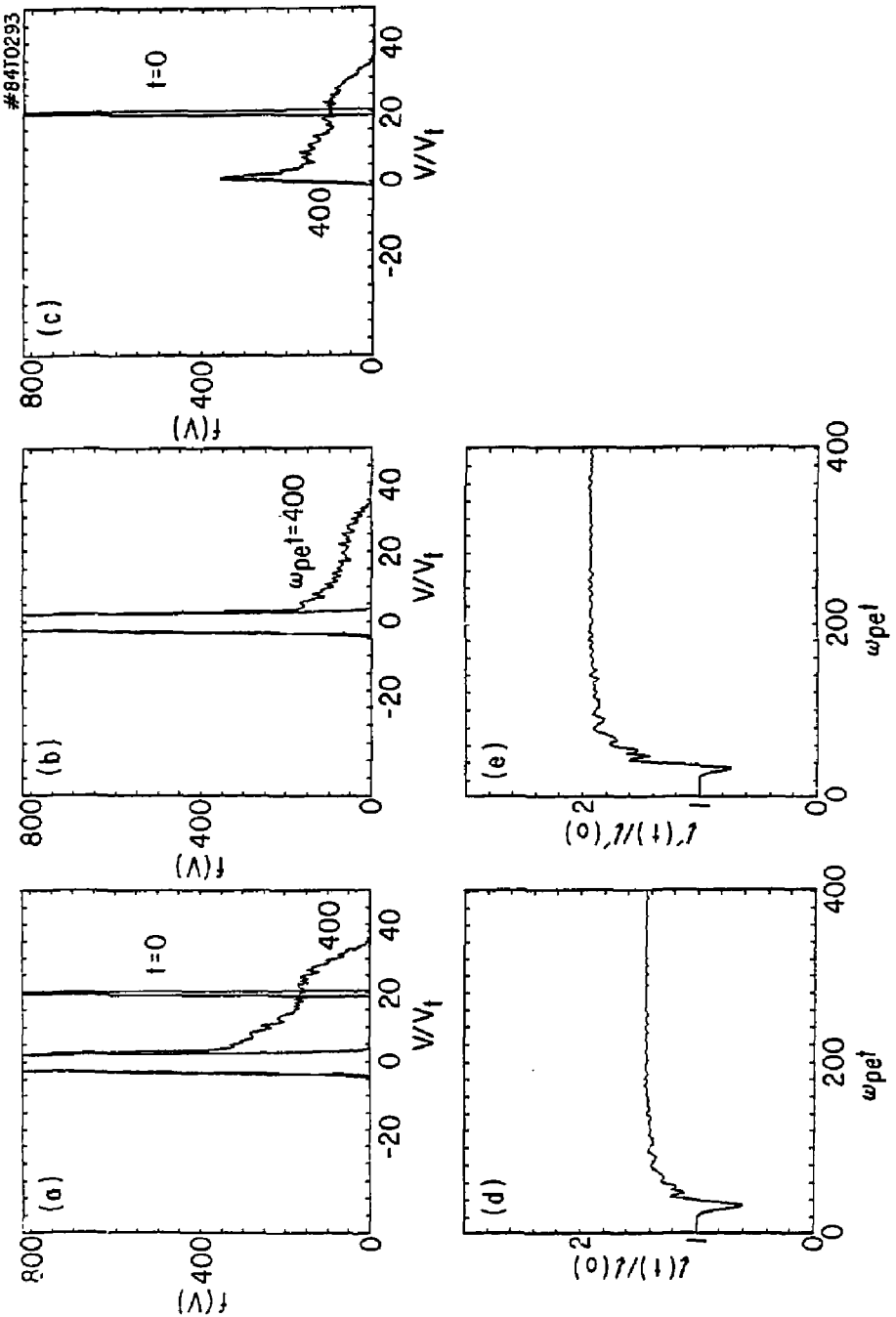

Fig. 12

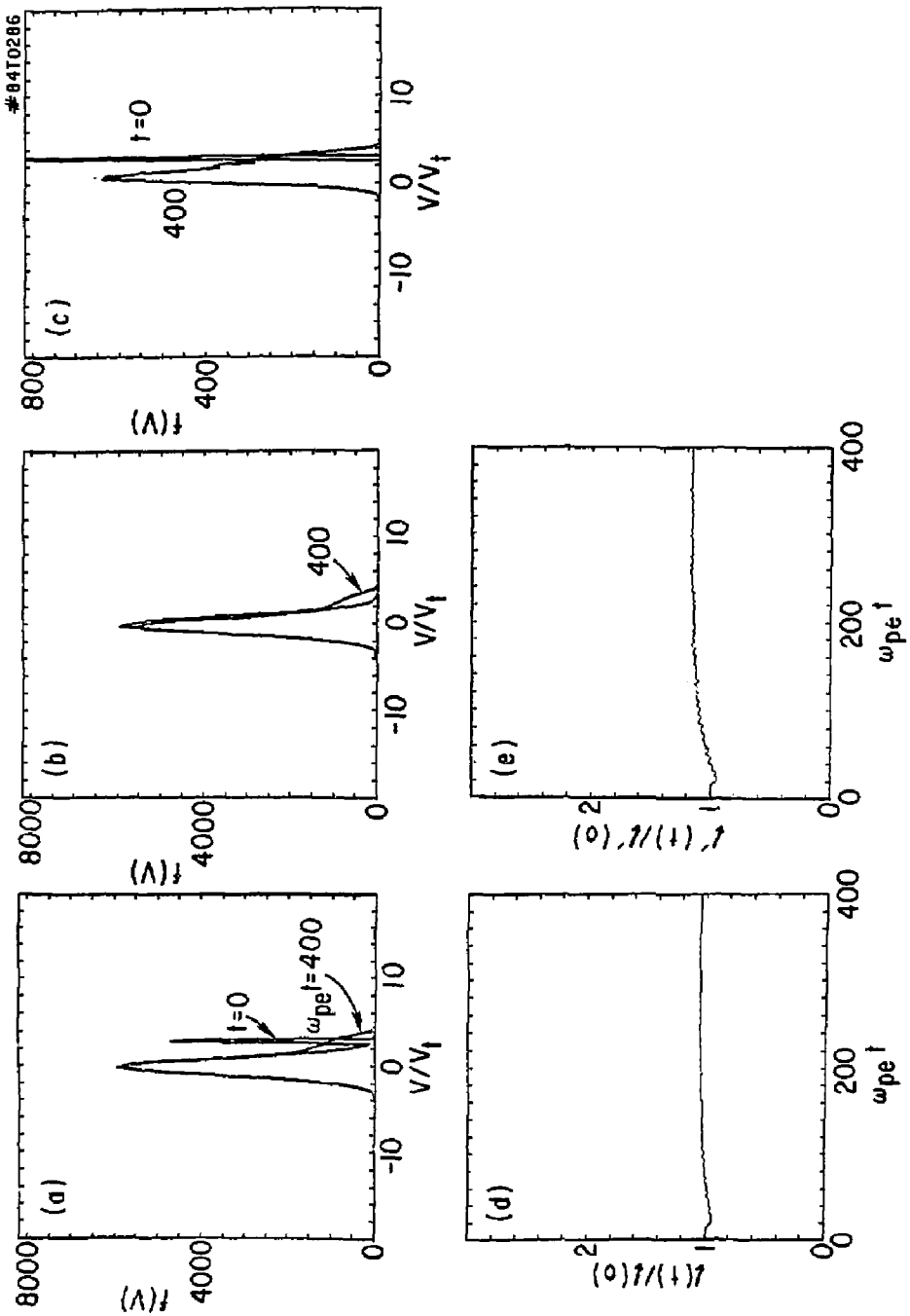

Fig. 13

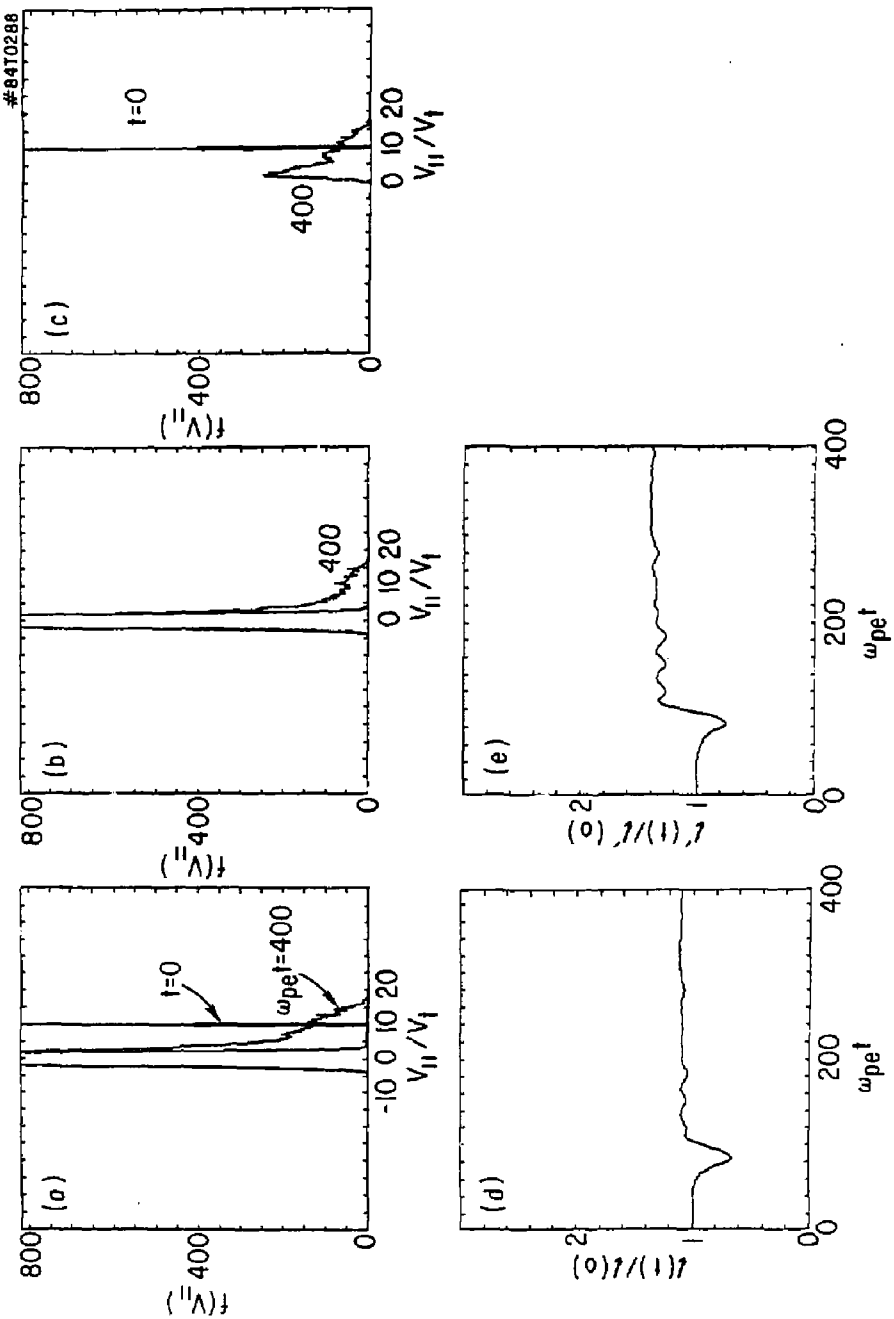

Fig. 14

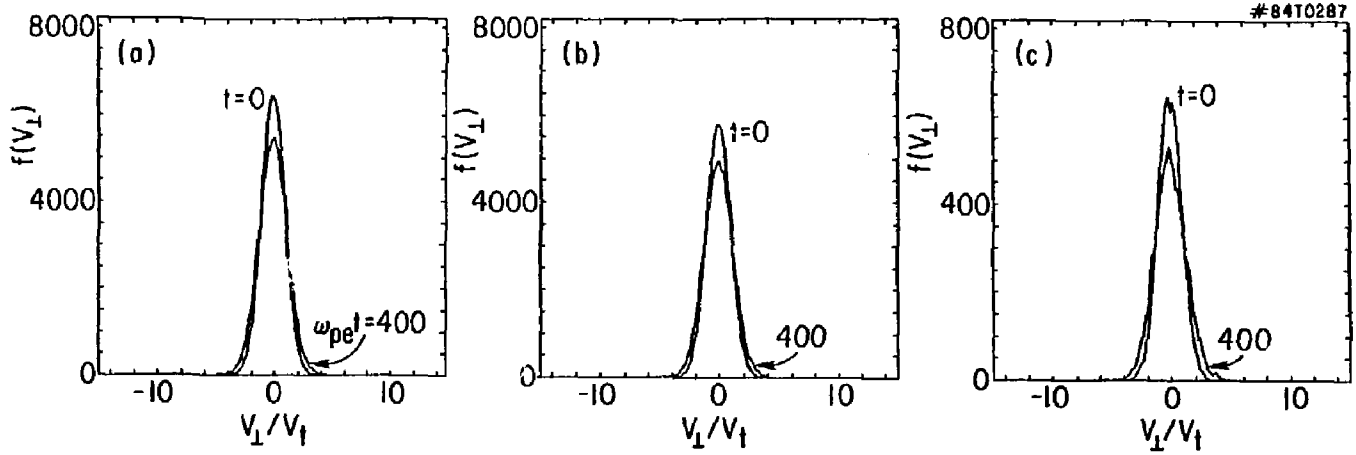
#84T0287
8000
(a)
t=0
f(V⊥)
4000
0
ωpet=400
-10
0
10
V⊥/Vt
8000
(b)
t=0
f(V⊥)
4000
0
400
-10
0
10
V⊥/Vt
800
(c)
t=0
f(V⊥)
400
0
400
-10
0
10
V⊥/Vt

Fig. 15

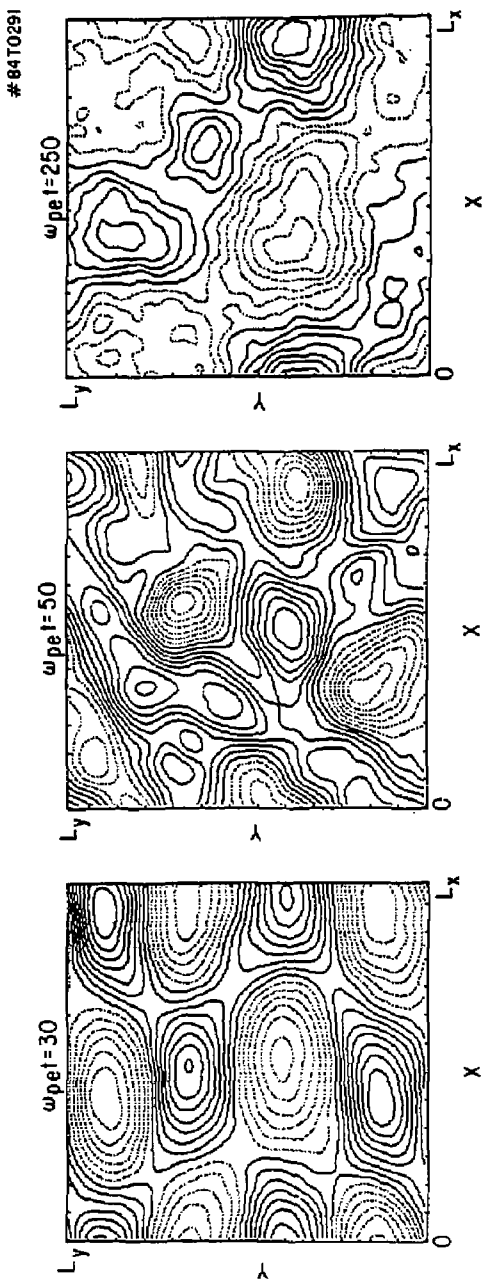

Fig. 16

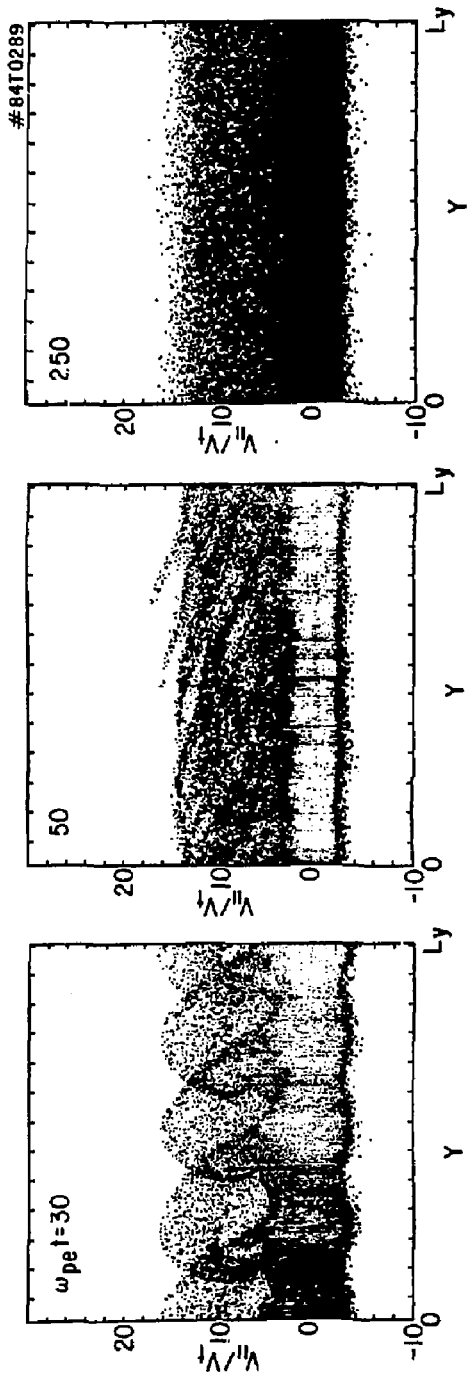

Fig. 17

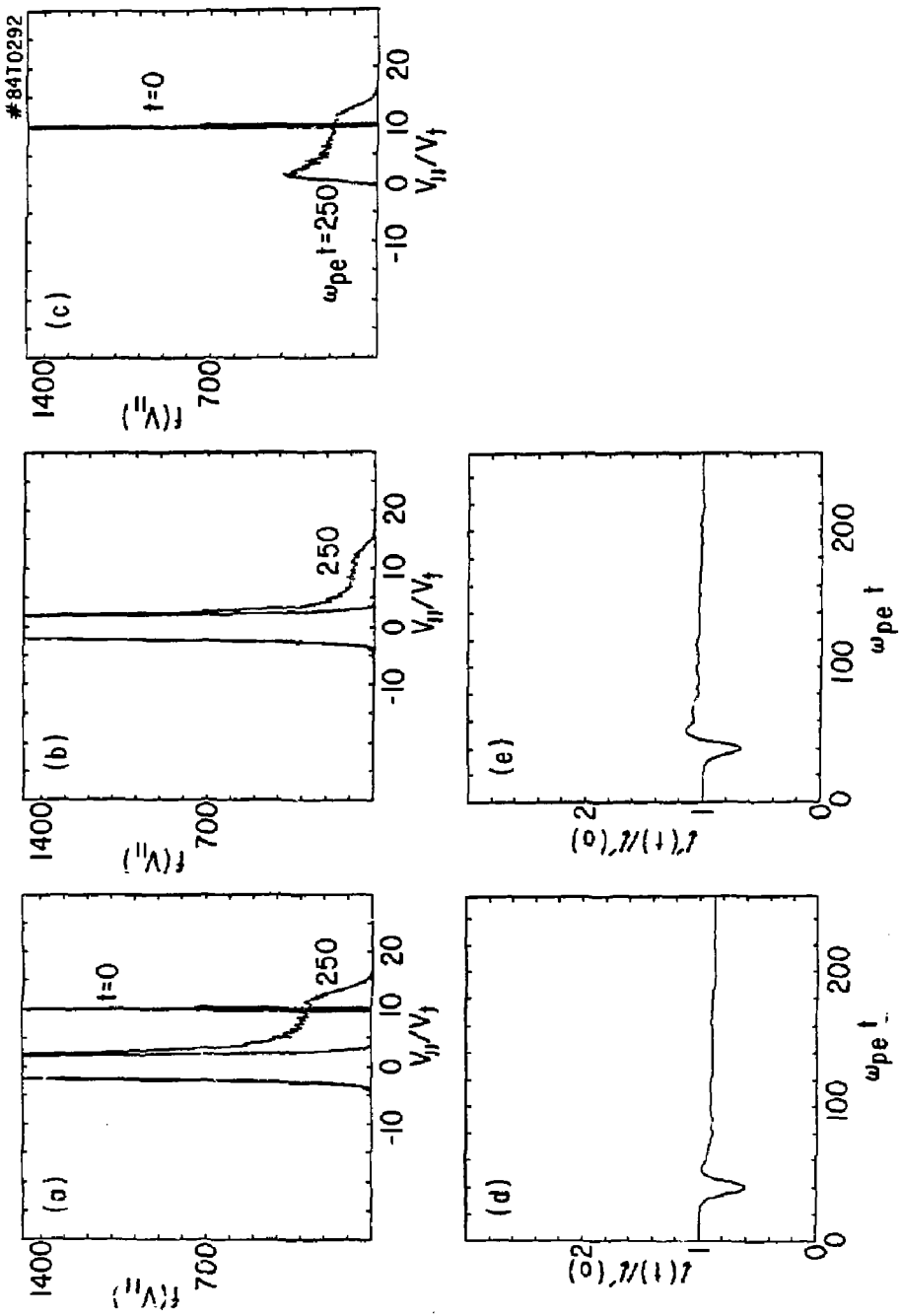

Fig. 18

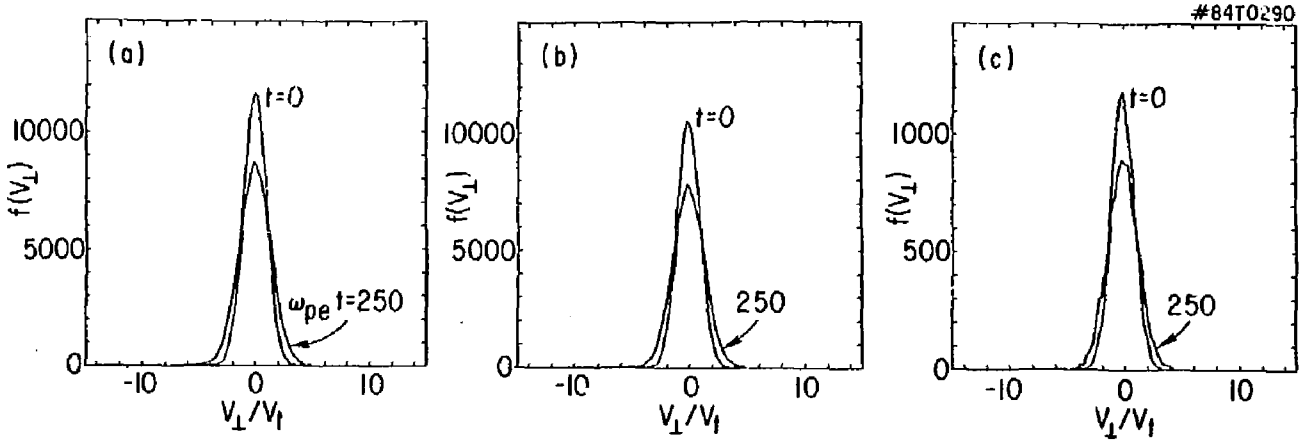
#84T0290
(a)
t=0
10000
5000
0
f(V⊥)
ωpe t=250
-10
0
10
V⊥/Vt
(b)
t=0
10000
5000
0
f(V⊥)
250
-10
0
10
V⊥/Vt
(c)
t=0
1000
500
0
f(V⊥)
250
-10
0
10
V⊥/Vt

Fig. 19

EXTERNAL DISTRIBUTION IN ADDITION TO 2-20

Plasma Res Lab, Austra Nat'l Univ, AUSTRALIA
Dr. Frank J. Paoloni, Univ of Wollongong, AUSTRALIA
Prof. I.R. Jones, Flinders Univ., AUSTRALIA
Prof. M.H. Brennan, Univ Sydney, AUSTRALIA
Prof. F. Cap, Inst Theo Phys, AUSTRIA
Prof. Frank Verheest, Inst theoretische, BELGIUM
Dr. D. Palumbo, Dg XII Fusion Prog, BELGIUM
Ecole Royale Militaire, Lab de Phys Plasmas, BELGIUM
Dr. P.H. Sakanaka, Univ Estadual, BRAZIL
Dr. C.R. James, Univ of Alberta, CANADA
Prof. J. Teichmann, Univ of Montreal, CANADA
Dr. H.M. Skarsgard, Univ of Saskatchewan, CANADA
Prof. S.R. Sreenivasan, University of Calgary, CANADA
Prof. Tudor W. Johnston, INRS-Energie, CANADA
Dr. Hannes Barnard, Univ British Columbia, CANADA
Dr. M.P. Bachynski, MPB Technologies, Inc., CANADA
Chalk River, Nucl Lab, CANADA
Zhengwu Li, SW Inst Physics, CHINA
Library, Tsing Hua University, CHINA
Librarian, Institute of Physics, CHINA
Inst Plasma Phys, Academia Sinica, CHINA
Dr. Peter Lukac, Komenskeho Univ, CZECHOSLOVAKIA
The Librarian, Culham Laboratory, ENGLAND
Prof. Schatzman, Observatoire de Nice, FRANCE
J. Radet, CEN-BP6, FRANCE
AM Dupas Library, AM Dupas Library, FRANCE
Dr. Tom Mual, Academy Bibliographic, HONG KONG
Preprint Library, Cent Res Inst Phys, HUNGARY
Dr. S.K. Trehan, Panjab University, INDIA
Dr. Indra Mohan Lal Das, Banaras Hindu Univ, INDIA
Dr. L.K. Chavda, South Gujarat Univ, INDIA
Dr. R.K. Chhajlani, Vikram Univ. INDIA
Dr. B. Dasgupta, Saha Inst, INDIA
Dr. P. Kaw, Physical Research Lab, INDIA
Dr. Phillip Rosenau, Israel Inst Tech, ISRAEL
Prof. S. Cuperman, Tel Aviv University, ISRAEL
Prof. G. Rostagni, Univ Di Padova, ITALY
Librarian, Int'l Ctr Theo Phys, ITALY
Miss Clelia De Palo, Assoc EURATOM-ENEA, ITALY
Biblioteca, del CNR EURATOM, ITALY
Dr. H. Yamato, Toshiba Res & Dev, JAPAN
Direc. Dept. Lg. Tokamak Dev. JAERI, JAPAN
Prof. Nobuyuki Inoue, University of Tokyo, JAPAN
Research Info Center, Nagoya University, JAPAN
Prof. Kyoji Nishikawa, Univ of Hiroshima, JAPAN
Prof. Sigeru Mori, JAERI, JAPAN
Library, Kyoto University, JAPAN
Prof. Ichiro Kawakami, Nihon Univ, JAPAN
Prof. Satoshi Itoh, Kyushu University, JAPAN
Dr. D.I. Choi, Adv. Inst Sci & Tech, KOREA
Tech Info Division, KAERI, KOREA
Bibliotheek, Fom-Inst Voor Plasma, NETHERLANDS
Prof. B.S. Liley, University of Waikato, NEW ZEALAND
Prof. J.A.C. Cabral, Inst Superior Tecn, PORTUGAL
Dr. Octavian Petrus, ALI CUZA University, ROMANIA
Prof. M.A. Hellberg, University of Natal, SO AFRICA
Dr. Johan de Villiers, Plasma Physics, Nucor, SO AFRICA
Fusion Div. Library, JEN, SPAIN
Prof. Hans Wilhelmson, Chalmers Univ Tech, SWEDEN
Dr. Lennart Ster..o, University of UMEA, SWEDEN
Library, Royal Inst Tech, SWEDEN
Centre de Recherchesen, Ecole Polytech Fed, SWITZERLAND
Dr. V.T. Tolok, Kharkov Phys Tech Ins, USSR
Dr. D.D. Ryutov, Siberian Acad Sci, USSR
Dr. G.A. Eliseev, Kurchatov Institute, USSR
Dr. V.A. Glukhikh, Inst Electro-Physical, USSR
Institute Gen. Physics, USSR
Prof. T.J.M. Boyd, Univ College N Wales, WALES
Dr. K. Schindler, Ruhr Universitat, W. GERMANY
Nuclear Res Estab, Julich Ltd, W. GERMANY
Librarian, Max-Planck Institut, W. GERMANY
Bibliothek, Inst Plasmaforschung, W. GERMANY
Prof. R.K. Janev, Inst Phys, YUGOSLAVIA